

UC San Diego

UC San Diego Electronic Theses and Dissertations

Title

The effects of pre-formed plasma on the generation and transport of fast electrons in relativistic laser-solid interactions

Permalink

<https://escholarship.org/uc/item/4df8p13t>

Author

Paradkar, Bhooshan S.

Publication Date

2012

Peer reviewed|Thesis/dissertation

UNIVERSITY OF CALIFORNIA, SAN DIEGO

**The effects of pre-formed plasma on the generation and transport of
fast electrons in relativistic laser-solid interactions**

A dissertation submitted in partial satisfaction of the
requirements for the degree
Doctor of Philosophy

in

Engineering Sciences (Engineering Physics)

by

Bhooshan S. Paradkar

Committee in charge:

Professor Farhat Beg, Chair
Professor Sergei Krasheninnikov, Co-Chair
Professor Thomas O'Neil
Professor Kevin Quest
Professor George Tynan

2012

Copyright
Bhooshan S. Paradkar, 2012
All rights reserved.

The dissertation of Bhooshan S. Paradkar is approved,
and it is acceptable in quality and form for publication
on microfilm and electronically:

Co-Chair

Chair

University of California, San Diego

2012

DEDICATION

Dedicated to my parents,
Smt. Vanita S. Paradkar and Late Shree. Shrikrishna S. Paradkar

EPIGRAPH

Bottomless wonders spring from simple rules ...repeated without end.

—Benoit Mandelbrot

TABLE OF CONTENTS

Signature Page	iii
Dedication	iv
Epigraph	v
Table of Contents	vi
List of Figures	viii
Acknowledgements	x
Vita and Publications	xii
Abstract of the Dissertation	xiii
Chapter 1 Introduction	1
1.1 Background	1
1.2 Motivation	2
1.3 Dissertation outline	5
1.3.1 Chapter 2 : A brief review of theory of relativistic intensity laser-solid interaction	5
1.3.2 Chapter 3 and 4 : Fast electron generation in the presence of pre-formed plasma	5
1.3.3 Chapter 5 : Effect of pre-formed plasma on fast electron transport	6
1.3.4 Chapter 6: Summary and Conclusions	7
Chapter 2 Review of theory of relativistic intensity laser-solid interaction	8
2.1 Single electron motion in laser field	9
2.2 Laser propagation in plasma	11
2.3 Laser absorption mechanisms and fast electrons generation	14
2.4 Electron beam transport through plasma	17
Chapter 3 Fast electron generation in the presence of pre-formed plasma	20
3.1 PIC modeling with immobile ions	21
3.2 Dynamics of electrons in the pre-formed plasma	26
3.3 Electron heating due to synergetic effects of EM radiation and electrostatic potential well	31
3.4 PIC modeling with mobile ions	36
3.5 Conclusions	39

Chapter 4	Mechanism of heating of pre-formed plasma electrons	42
4.1	Electron motion inside deep potential well	43
4.2	Electron heating in finite depth potential well	49
4.3	Conclusions	50
Chapter 5	Fast electron transport studies in presence of long scale length pre-formed plasma	51
5.1	Introduction	52
5.2	Hydrodynamic modeling of the pre-plasma creation . . .	55
5.3	Fast electron transport modeling with hybrid PIC code, LSP	58
5.3.1	LSP simulation set up	58
5.3.2	Hybrid PIC simulation results and discussion . . .	63
5.4	Conclusions	69
Chapter 6	Conclusions	72
6.1	Summary and Conclusions	72
6.2	Future Work	73
Appendix A	Derivation of Poincare Mapping equations 4.9 and 4.10	75
Bibliography	79

LIST OF FIGURES

Figure 1.1:	Experimentally measured electron spectrum with and without pre-formed plasma	3
Figure 1.2:	Numerically simulated fast electron energy spectrum	4
Figure 2.1:	Schematic for laser filamentation and self-focusing instability .	13
Figure 2.2:	PIC simulations of laser filamentation	14
Figure 3.1:	Schematic of PIC simulations for pre-formed plasma studies . .	23
Figure 3.2:	(a) Electron energy distribution inside the target for laser intensity of 10^{20} W/cm ² and 15 μ m pre-plasma scale-length (b) Cumulative heat flux carried by the electrons inside the target.	25
Figure 3.3:	(a) Simulated electron energy distribution inside target (b) Mean energy dependence on laser intensity and pre-formed plasma scale-length	26
Figure 3.4:	Laser interaction with pre-formed plasma during initial stages of laser propagation through under-dense plasma.	29
Figure 3.5:	Phase-space density and electrostatic potential (solid red line) evolution as laser starts heating the pre-formed plasma.	30
Figure 3.6:	Comparison of phase space plots for (a) 5 μ m and (b) 15 μ m pre-formed plasma scale lengths (Laser intensity = 10^{20} W/cm ²).	32
Figure 3.7:	Single electron phase-space trajectories with counter propagating EM waves and longitudinal electric field	34
Figure 3.8:	Dynamics of plasma heating due to counter propagating EM waves with and without potential well (PIC simulations).	36
Figure 3.9:	Dynamics with mobile ions ($L_p = 5 \mu$ m; $I_L = 10^{20}$ W/cm ²).	38
Figure 3.10:	Laser absorption for various initial pre-formed plasma scale-length and laser intensities.	39
Figure 4.1:	Profiles of potential well chosen to demonstrate the electron heating in the pre-formed plasma	43
Figure 4.2:	Comparison of poicare map obtained from numerical calculations and analytical results obtained from Eq. (8) and (9).	47
Figure 4.3:	Poincare map in (γ, ϕ) space for different values of a_0/E_z . Transition from strictly periodic motion (Fig. (a) and (b)) to stochastic motion (Fig. (d)) with increasing values of a_0/E_z is clearly demonstrated here.	48
Figure 4.4:	Average energy of electrons inside potential well vs time (numerical calculations) confirming $t^{1/3}$ dependance predicted by Eq.(4.12).	48

Figure 4.5:	Energy distribution functions for total energy (Fig. (a)) and parallel energy (Fig. (b)) of electrons escaping the finite depth potential well for different a_0 values such that elementary energy-step size, a_0^2/E_z is constant.	49
Figure 5.1:	Experimental study of effect of long pre-formed plasma on the fast electrons transport.	53
Figure 5.2:	Results of radiation hydrodynamics simulations of generation of pre-formed plasma in the experiment.	57
Figure 5.3:	Set-up for hybrid PIC simulations to study the fast electrons transport	62
Figure 5.4:	Results of early stages of fast electrons transport	64
Figure 5.5:	Deflection of fast electrons, traveling along the target front surface into the pre-formed plasma by magnetic field	65
Figure 5.6:	Fast electron refluxing in the coronal plasma back to solid target.	66
Figure 5.7:	Excitation of axial electric field resulting in pulling back of fast electrons to the solid target	67
Figure 5.8:	Comparison of simulation results with the experiments	69
Figure 5.9:	Fast electron density comparison at 1.8 ps for 10° and 60° half angle beam divergence.	70
Figure 5.10:	Simulation results without pre-formed plasma	70
Figure A.1:	Profiles of potential well chosen to demonstrate the electron heating in the pre-formed plasma	76

ACKNOWLEDGEMENTS

This thesis is a result of collective efforts of a lot of people around me who have helped me, either directly or indirectly, in reaching this stage of my journey. I can not proceed any further without thanking all these people who have so far made this journey possible.

First of all, I would like to give my sincere thanks to my advisor Prof. Farhat Beg and co-advisor Prof. Sergei Krasheninnikov for their constant guidance and inspiration all through out my graduate studies. I consider myself really fortunate to have gotten the opportunity to work with these two not just brilliant physicist but also great human beings. The patience and confidence they showed in me also played a role in gaining some self-confidence. Also, thanks are due to my PhD thesis committee members Prof. O’Neil, Prof. Tynan and Prof. Quest for their valuable time and useful suggestions/comments on my thesis.

I would also like to thank all my colleagues here at the UCSD’s ‘High Energy Density Physics’ Group. A friendly, supportive atmosphere in the group makes this group a great place to do physics !! In particular, special thanks to Dr. Mingsheng Wei, Dr. Rich Stephens, Dr. Toshinori Yabuuchi, Prof. Malcolm Haines for their valuable advising and guidance during my PhD.

Last but not the least, the importance of my family and friends in helping me in achieving the balance of professional and personal life can’t be undermined. I think it would be a futile exercise to put it in words how much I owe to my parents and my sisters to reach this stage of my life. As I begin the writing of this doctoral thesis, I can not forget all the sacrifices these wonderful people in my family have done for me. With the recent addition of my fiancée, Bhavna to the family I am experiencing a new dimension of life. The emotional support I have experienced from her during last one year has been instrumental. Also, I would like to thank all my close friends, Bishakh, Bhupi, Justin, Kowsik, Drew, Dhritiman, Neelmani, Subhra, Narsimha, who have become in a way my extended family in La Jolla away from the family.

Finally, I would like to give a word of thanks to all my co-authors for allowing me to use the following papers as a part of my thesis :

B. S. Paradkar, S. I. Krasheninnikov and F. N. Beg, “Mechanism of pre-formed plasma electrons heating in relativistic laser-solid interaction”, submitted to *Phys. Rev. Lett.*.

B.S.Paradkar, M.S.Wei, T. Yabuuchi, R.B.Stephens, M.G. Haines, S.I. Krasheninnikov and F.N.Beg, “Numerical modeling of fast electrons generation in presence of pre-formed plasma in laser-matter interaction at relativistic intensity”, *Phys. Rev. E* **83** 046401, 2011.

B.S.Paradkar, M.S. Wei, T. Yabuuchi, R. B. Stephens, J. T. Larsen and F. N. Beg, “Numerical modeling of fast electrons transport in short pulse laser-solid interactions with long scale-length pre-formed plasma”, *Plasma Physics and Controlled Fusion* **52** 125003, 2010.

VITA

2002	Bachelor of Electrical Engineering, University of Mumbai, India
2009	Master of Science in Engineering Physics, University of California, San Diego
2007-2011	Graduate Research Assistant, University of California, San Diego
2012	Doctor of Philosophy in Engineering Sciences (Engineering Physics), University of California, San Diego

PUBLICATIONS

B. S. Paradkar, S. I. Krasheninnikov and F. N. Beg, “Mechanism of pre-formed plasma electrons heating in relativistic laser-solid interaction”, submitted to *Phys. Rev. Lett.*.

B.S.Paradkar, M.S.Wei, T. Yabuuchi, R.B.Stephens, M.G. Haines, S.I. Krasheninnikov and F.N.Beg, “Numerical modeling of fast electrons generation in presence of pre-formed plasma in laser-matter interaction at relativistic intensity”, *Phys. Rev. E* **83** 046401, 2011.

B.S.Paradkar, M.S. Wei, T. Yabuuchi, R. B. Stephens, J. T. Larsen and F. N. Beg, “Numerical modeling of fast electrons transport in short pulse laser-solid interactions with long scale-length pre-formed plasma”, *Plasma Physics and Controlled Fusion* **52** 125003, 2010.

T. Yabuuchi, **B.S.Paradkar**, M.S. Wei, J.A.King, F. N. Beg, R. B. Stephens, et al., *Physics of Plasmas* **17** 060704, 2010.

B.S.Paradkar, J. Ghosh, P.K. Chattopadhyay, R.L. Tanna et al., *Physics of Plasmas* **17** 092504, 2010.

ABSTRACT OF THE DISSERTATION

The effects of pre-formed plasma on the generation and transport of fast electrons in relativistic laser-solid interactions

by

Bhooshan S. Paradkar

Doctor of Philosophy in Engineering Sciences (Engineering Physics)

University of California, San Diego, 2012

Professor Farhat Beg, Chair
Professor Sergei Krasheninnikov, Co-Chair

In this thesis we present the dynamics of relativistic fast electrons produced in the laser-solid interactions at the intensities greater than 10^{18} W/cm². In particular, the effects of pre-formed plasma in front of a solid target on the generation and transport of these fast electrons is studied. The presence of such a pre-formed plasma is ubiquitous in almost all the present short pulse high intensity laser-solid interaction experiments.

First, the generation of fast electrons in the presence of pre-formed plasma of varying density scale-lengths is studied with the help of Particle In Cell (PIC) simulations. It is shown that the fast electrons energy increases with the increasing

pre-formed plasma, consistent with the experimental observations. The possible mechanism of generation of such energetic electrons is studied. It is proposed that the interaction of plasma electrons with the laser in the presence of ambipolar electric field, generated due to the laser heating, can result in the electron acceleration beyond laser ponderomotive energy. The analytical and numerical studies of this heating mechanism are presented.

In the second part of thesis, the influence of pre-formed plasma on the fast electrons transport is studied. Especially the physics of refluxing of these fast electrons due to the excitation of electrostatic sheath fields inside the pre-formed plasma is investigated. It is shown that this refluxing is responsible for the ‘annular ring shaped’ copper $K\alpha$ x-ray emission observed in the recent high intensity laser-solid experiments.

Chapter 1

Introduction

1.1 Background

Intense electron beams produced by relativistic laser interaction with solid targets are studied extensively, both theoretically and experimentally, by the plasma physics community. The interests are mainly driven by the potential use of these electron beams in a number of applications such as fast ignition [Key et al., 2008, Tabak et al., 1994], ion acceleration [Hatchett et al., 2000, Wilks et al., 2001], electron-positron pair production [Liang et al., 1998], high energy K_α and Gamma ray source [Courtois et al., 2009, Park et al., 2006], table-top electron acceleration [Tajima and Dawson, 1979] etc. The electron energies needed for optimal performance depend upon the application under consideration. For example, the required electron energy is in the range 1-3 MeV [Key et al., 2008] for fast ignition; whereas typically much higher electron energies are needed for pair production. Therefore, clear understanding of generation and transport of these electrons is crucial for optimal performance of each of the above-mentioned application.

The present work concerns the dynamics of such relativistic electrons produced in laser-solid interactions. In particular, the influence of ‘pre-formed plasma’ [Adumi et al., 2004] in front of a solid target on fast electron generation and transport is studied here. The name ‘pre-formed plasma’ is derived from the fact that such plasma is created before the arrival of main relativistic intensity laser due to the ablation of solid target by the laser pre-pulse [Chen et al., 2007], i.e. the

nano second time scale pedestal in front of main laser. Such studies are extremely important for understanding the dynamics of fast electrons in laser-solid interactions as pre-formed plasma of varying scale-length is almost always present in the experiments. Here, we have performed the theoretical and numerical investigation of the role of such a pre-formed plasma in relativistic laser-solid interactions.

1.2 Motivation

Recent experiments suggest that the presence of pre-formed plasma in front of solid target can strongly influence the fast electrons generation and transport. The density scale-length of such plasma could be as high as 10-15 μm for a typical energy contrast of 10^{-5} between the pre-pulse and energetic main pulses of energies 10-100 kJ. The experiment with planar targets [Yabuuchi et al., 2010] showed that the energetic fast electrons with energies much greater than the ponderomotive potential [Wilks et al., 1992] are generated in the presence of pre-formed plasma with a density scale-length of approximately 10 μm (see figure 1.1). The electrons spectrum in red here is produced in presence of long scale-length pre-formed plasma and gray and blue spectrum are produced when there no significant pre-formed plasma.

Also, the experiments with the cone shaped targets [Baton et al., 2008, MacPhee et al., 2010, Van Woerkom et al., 2008] have shown that the fast electron generation is significantly modified by the presence of long scale pre-plasma inside the cone. The fast electrons coupling to the solid target was affected due to the presence of pre-formed plasma inside the cone [Baton et al., 2008]. This was due to the increased transport distance for the fast electrons caused by the expansion of plasma in front of the target. This resulted in shifting of critical density surface away from the solid target. In case of proton acceleration experiments, increase in maximum proton energy was reported with increase in pre-pulse energy [Kaluza et al., 2004, Yogo et al., 2007]. This increase in maximum energy was attributed to the increase in absorption efficiency of the main pulse due to the presence of longer pre-formed plasma in front of a target.

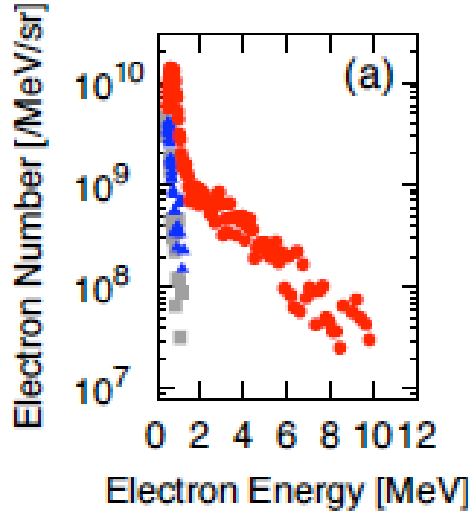


Figure 1.1: Experimentally measured electron spectrum with and without long scale-length pre-formed plasma (laser intensity = 2×10^{18} W/cm²) [Yabuuchi et al., 2010].

The generation of fast electron in presence of pre-plasma is addressed in number of theoretical and numerical publications [Andreev et al., 2003, Cai et al., 2010, Kemp et al., 2009, Lee et al., 2004, Lefebvre and Bonnaud, 1997, Mishra et al., 2009, Nuter et al., 2008, Pukhov et al., 1999, Sentoku et al., 2002]. In many cases the fast electrons spectrum generated during laser plasma interaction is characterized by a mean energy of electrons that is referred as ‘hot electron temperature’, T_{hot} . In general, Particle In Cell (PIC) simulations predict increase in T_{hot} and laser absorption with increase in pre-plasma scale-length (e.g. [Kemp et al., 2009, Mishra et al., 2009]), consistent with the experimental observations. The fast electrons mean energy is found to be below ponderomotive energy for extremely steep density gradients, [Sherlock, 2009] whereas in the case of long pre-plasma scale-lengths, the observed mean energies are well beyond ponderomotive energies (refer figure 1.2) [Kemp et al., 2009] .

In addition to the discrepancy about the mean energy of the generated fast electrons, the situation is further complicated by the fact that the measured electrons spectrum shows distinct departure from single temperature maxwellian distribution. This may be attributed to the different heating mechanisms that

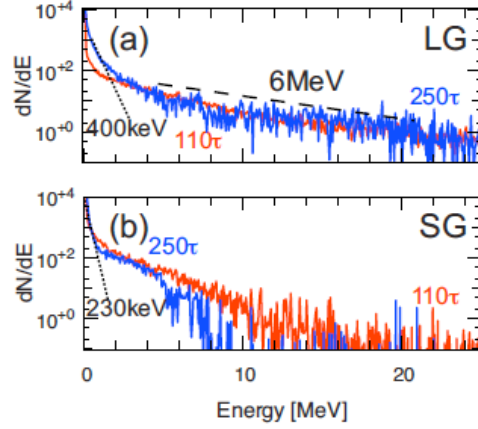


Figure 1.2: Numerically simulated fast electron energy spectrum for (a) Long density gradient ($3.25 \mu m$) (b) Small density gradient ($0.85 \mu m$). [Kemp et al., 2009].

might be playing dominant role depending upon the pre-plasma scale-length. It is proposed that dominant heating mechanism for small and long scale-length pre-plasma can be $J \times B$ heating and stochastic heating respectively [Nuter et al., 2008]. In case of steep density profiles, the electrostatic potential well is produced due to the charge separation near relativistic critical density surface play a crucial role in decreasing the energy of the fast electrons entering into solid targets [Sherlock, 2009]. For the steep density gradients, PIC simulations have reported the small-scale ($\sim c/\omega_{pe}$, collisionless skin-depth) blob-like formation close to critical density [Mishra et al., 2009]. It is also pointed out that the ‘high-energy tail’ of fast electrons distribution can be due to the combination of counter-propagating EM waves and longitudinal plasma waves [Kemp et al., 2009, Lefebvre and Bonnaud, 1997].

Thus, although the experimental evidences clearly demonstrate that the presence of pre-formed plasma can significantly affect the relativistic intensity laser-solid interaction, the clear theoretical understanding about the role of pre-formed plasma is yet to emerge. In this thesis, we have addressed some of these issues theoretically and numerically with the help of Particle In Cell (PIC) simulations. In particular, the role of ambipolar electric field, present inside pre-formed plasma, on electron heating is investigated for the first time. The discussion in this thesis

is mainly applicable for the picosecond time scale laser interaction with plasma where such ambipolar fields can be created due to the laser heating.

1.3 Dissertation outline

Outline of the thesis is as follows :

1.3.1 Chapter 2 : A brief review of theory of relativistic intensity laser-solid interaction

This chapter gives a short review of basic physics of fast electron generation and transport relevant to laser-solid interaction. Topics such as single electron motion in an electromagnetic field, laser propagation in plasma, different laser absorption mechanisms, the setting up of return current due to fast electron beam propagation through plasma are covered. This physics is considered essential to understand the dynamics of fast electrons in the presence of plasma.

1.3.2 Chapter 3 and 4 : Fast electron generation in the presence of pre-formed plasma

These chapters address the role of pre-formed plasma on the generation of fast electrons in laser-solid interactions. Chapter 3 describes the systematic study of fast electron generation for different pre-formed plasma scale-lengths ($1\ \mu m$, $5\ \mu m$, $15\ \mu m$) and laser intensities (10^{19} W/cm^2 , 10^{20} W/cm^2 , 10^{21} W/cm^2) performed with the help of 1-D PIC code LSP [Welch et al., 2001, 2006]. Increase in the fast electron mean energy with increasing pre-formed plasma scale-length is reported. Detailed dynamics of electrons in pre-plasma and their heating mechanism is given in this chapter.

The role of longitudinal ambipolar electric field on pre-formed plasma electron heating is addressed in chapter 4. The theoretical study of stochastic heating of electrons in the presence of this electric field is performed by analyzing the single electron motion. The transition from regular(periodic) to stochastic regime due to

the presence of longitudinal electric field is demonstrated. Finally, it is shown that the electrons in pre-formed plasma can be heated beyond the laser ponderomotive energies in the stochastic regime.

This work is also described in the following papers :

- (1) **B.S.Paradkar**, M.S.Wei, T. Yabuuchi, R.B.Stephens, S.I. Krasheninnikov and F.N.Beg, “Numerical modeling of fast electrons generation in presence of pre-formed plasma in laser-matter interaction at relativistic intensity”, *Phys. Rev. E* **83** 046401, 2011.
- (2) **B. S. Paradkar**, S. I. Krasheninnikov and F. N. Beg, “Mechanism of pre-formed plasma electrons heating in relativistic laser-solid interaction”, submitted to *Phys. Rev. Lett.*.

1.3.3 Chapter 5 : Effect of pre-formed plasma on fast electron transport

This chapter describes numerical modeling of fast electron transport in presence of pre-formed plasma. Specifically, the physics of the annular ring observed in Copper K_α x-ray emission [Yabuuchi et al., 2010] due to the fast electrons transport through multilayered solid target is explained. Such emission was seen in the experiment only in presence of long scale-length pre-formed plasma. The reflection of fast electrons in the pre-formed plasma when fast electron density becomes comparable to background density due to space-charge electric field is clearly demonstrated with the help of numerical simulations performed with the hybrid PIC code LSP. This work is published in:

- (1) **B.S.Paradkar**, M.S. Wei, T. Yabuuchi, R. B. Stephens, J. T. Larsen and F. N. Beg, “Numerical modeling of fast electrons transport in short pulse laser-solid interactions with long scale-length pre-formed plasma”, *Plasma Physics and Controlled Fusion* **52** 125003, 2010.

1.3.4 Chapter 6: Summary and Conclusions

Finally summary and conclusion of this thesis is given in chapter 6. Also, the future work in this topic the author would like to pursue is mentioned here.

Chapter 2

Review of theory of relativistic intensity laser-solid interaction

Laser-solid interaction studies have made great progress in the last two decades since the invention of *Chirped Pulse Amplification* (CPA) technique [Maine et al., 1988, Strickland and Mourou, 1985]. This technique allowed construction of modern day lasers with intensities above 10^{18} W/cm². Lasers with such high intensities have enabled us to probe the interaction of matter with light where the electron motion is relativistic. This can be seen from observing that a single electron in presence of oscillating electric field, $E = E_0 \sin \omega t$ will quiver with a velocity, V_{osc} given by

$$\frac{V_{osc}}{c} = \frac{eE_0}{m\omega c} \cos \omega t = a_0 \cos \omega t \quad (2.1)$$

Note that $a_0 = \frac{eE_0}{m\omega c}$ is the normalized vector potential. Therefore, when $a_0 \gtrsim 1$ the electron oscillation velocity becomes relativistic i.e. $V_{osc} \lesssim c$. Since the laser intensity (Poynting flux) is given by $I_L = cE_0^2/(8\pi)$, the relativistic regime can be estimated as

$$a_0^2 = \frac{I_L (W/cm^2) \lambda_L^2 (\mu m^2)}{1.37 \times 10^{18}} \gtrsim 1 \quad (2.2)$$

Therefore for 1 μm laser with intensities greater than 10^{18} W/cm², the relativistic corrections must be added to the electron motion. With this intensity range in

mind, we now review some of the basic physics of short pulse high intensity laser plasma interactions.

2.1 Single electron motion in laser field

We begin our discussion by reviewing the single electron motion in presence of electromagnetic radiation. Understanding this ‘single particle’ description is very important although in plasma physics typically ‘collective effects’ are considered to play a dominant role. Especially for the interaction of relativistic intensity laser with the underdense plasma, the single particle approach is very helpful.

The Lagrangian for a charge (charge e , mass m) in an electromagnetic field is given by [Landau and Lifshitz, 2010]

$$L(\vec{V}, \vec{r}, t) = -mc^2 \sqrt{1 - \frac{V^2}{c^2}} + \frac{e}{c} \vec{A} \cdot \vec{V} - e\phi \quad (2.3)$$

where $\vec{A}(\vec{r}, t)$ and $\phi(\vec{r}, t)$ are the vector and scalar potentials of the field respectively. Then the canonical momentum, \vec{P} is defined as

$$\vec{P} = \frac{\partial L}{\partial \vec{V}} = \frac{m\vec{V}}{\sqrt{1 - \frac{V^2}{c^2}}} + \frac{e}{c} \vec{A} = \vec{p} + \frac{e}{c} \vec{A} \quad (2.4)$$

Here $\vec{p} = \gamma m \vec{V}$ is the ordinary (mechanical) momentum of the electron, γ being the Lorentz factor. Remembering the momentum equation $d\vec{P}/dt = \partial L / \partial \vec{r}$, we now can write equation of mechanical momentum as [Angus and Krasheninnikov, 2009]

$$\frac{d}{dt} [\gamma m \vec{V}] = -e \nabla \phi + \frac{e}{c} \left[\nabla \vec{A} \cdot \vec{V} - \frac{d\vec{A}}{dt} \right] \quad (2.5)$$

Note that by substituting $E = -\nabla \phi - \frac{1}{c} \frac{\partial \vec{A}}{\partial t}$ and $\frac{d\vec{A}}{dt} = \frac{\partial \vec{A}}{\partial t} + (\vec{V} \cdot \nabla) \vec{A}$ we recover usual Lorentz force equation.

Now, we consider simple one dimensional case where $\vec{A} \equiv \vec{A}(z, t) \equiv (A_\perp, A_z)$, $\phi \equiv \phi(z, t)$ and $\vec{r} \equiv (r_\perp, z)$. Noting that $(\nabla \vec{A} \cdot \vec{V})_j = \sum_{i=1}^3 (\partial A_i / \partial r_j) V_i$, we get

following relations for parallel (z) and perpendicular (r_\perp) directions.

$$\frac{d}{dt} \left[\gamma m V_\perp + \frac{e}{c} A_\perp \right] = 0 \quad (2.6)$$

$$\frac{d}{dt} [\gamma m V_z] = e E_z + \frac{e}{c} \left[V_\perp \frac{\partial A_\perp}{\partial z} \right] \quad (2.7)$$

This shows that in one dimensional case, canonical momentum is conserved in the perpendicular direction. Integrating Eq. (2.6) and taking $V_\perp(0) = A_\perp(0) = 0$ we can reduce Eq.(2.7) into

$$\frac{d}{dt} [\gamma m V_z] = e E_z - \frac{e^2}{2\gamma m c^2} \frac{\partial A_\perp^2}{\partial z} \quad (2.8)$$

The second term on the right hand side represents the nonlinear ‘relativistic ponderomotive force’ on the charge particle. The time averaging of this force is typically associated with the the potential called ‘ponderomotive potential’, ϕ_p . Finally the energy conservation equation can be written as

$$\frac{d}{dt} [\gamma m c^2] = e \vec{E} \cdot \vec{V} = e E_z V_z + \frac{e^2}{2\gamma m c^2} \frac{\partial A_\perp^2}{\partial t} \quad (2.9)$$

For an electromagnetic radiation (ω, k) , we apply normalization as : $t \rightarrow \omega t$, $z \rightarrow kz$, $p \rightarrow p/mc$, $V \rightarrow V/c$, $\hat{A} \rightarrow eA/(mc^2)$ and $E \rightarrow eE/(mc\omega)$. With this we can write relativistic electron dynamics in non-dimensional form as

$$\begin{aligned} \frac{d}{dt} [\gamma V_\perp - \hat{A}_\perp] &= 0 \\ \frac{d}{dt} [\gamma V_z] &= -E_z - \frac{1}{2\gamma} \frac{\partial \hat{A}_\perp^2}{\partial z} \\ \frac{d\gamma}{dt} &= -E_z V_z + \frac{1}{2\gamma} \frac{\partial \hat{A}_\perp^2}{\partial t} \end{aligned} \quad (2.10)$$

For $E_z = 0$ and plane electromagnetic wave $\hat{A}_\perp \equiv \hat{A}_\perp(t - z)$, the parallel momentum equation and energy conservation equation can be combined to give another constant of motion as

$$\frac{d}{dt} [\gamma - p_z] = \frac{d}{dt} [\gamma (1 - V_z)] = 0 \quad (2.11)$$

Thus combining the constant of motion, $\gamma - p_z = \Delta$ with the relation $\gamma^2 = 1 + p_z^2 + p_\perp^2$ we get

$$p_z = \frac{1 - \Delta^2 + p_\perp^2}{2\Delta} \quad (2.12)$$

Noting that $p_\perp = \hat{A}_\perp$ (from conservation of canonical momentum in the perpendicular direction), for an electron initially at rest ($\Delta = 1$) and linearly polarized light ($\hat{A}_\perp = a_0 \cos(t - z) = a_0 \cos \tau$), we can calculate p_z and p_\perp as

$$\begin{aligned} p_z &= \frac{a_0^2}{4} [1 + \cos 2\tau] \\ p_\perp &= a_0 \cos \tau \end{aligned} \quad (2.13)$$

The above equation demonstrates that the longitudinal momentum of electron in the presence of linearly polarized light has a secular component and a non-stationary component which oscillates at twice the light frequency. This so called ‘ 2ω ’ oscillation is characteristic of a linearly polarized light. On the other hand, for the circularly polarized light ($\hat{A}_\perp = \frac{a_0}{\sqrt{2}} [\cos \tau \hat{x} \pm \sin \tau \hat{y}]$), we get $\hat{A}_\perp^2 = \text{constant}$. In other words, ‘ 2ω ’ oscillations are absent for the circularly polarized light. Therefore, for circular polarization we have,

$$\begin{aligned} p_z &= \frac{a_0^2}{4} \\ p_x &= \frac{a_0}{\sqrt{2}} \cos \tau \\ p_y &= \pm \frac{a_0}{\sqrt{2}} \sin \tau \end{aligned} \quad (2.14)$$

Thus, because of the constant drift along the longitudinal direction, the ponderomotive potential can be defined as $\phi_p \sim 0.5 \left(\sqrt{1 + a_0^2} - 1 \right)$. For example, for a circularly polarized laser with intensity of 10^{19} W/cm^2 , the electron should acquire the energy $E \sim \phi_p \sim 960 \text{ keV}$.

2.2 Laser propagation in plasma

Having analyzed the electron motion in the presence of relativistic intensity laser, we now turn our attention to the topic of propagation of laser through

plasma. Due to the presence of pre-formed plasma of varying density scale-length in almost all the laser-solid experiments, the laser has to propagate through plasma before it finally hits the solid surface. Therefore, understanding of light propagation through plasma is very important. This topic is extensively reviewed by William Kruer[Kruer, 2003].

The dispersion relation for an electromagnetic wave (ω, k) propagating through plasma is given by

$$\omega^2 = \omega_{pe}^2 + k^2 c^2 \quad (2.15)$$

ω_{pe} is the electron plasma frequency. Therefore, the refractive index of the plasma η_r can be expressed as

$$\eta_r \equiv \sqrt{\epsilon} \equiv \sqrt{1 - \frac{\omega_{pe}^2}{\omega^2}} \quad (2.16)$$

ϵ is the dielectric constant of the plasma. This naturally leads to the definition of ‘critical density’ n_{cr} beyond which the laser with frequency ω_L can’t propagate ($k = 0$) as

$$n_{cr} = \frac{m_e \omega_L^2}{4\pi e^2} \quad (2.17)$$

in practical units, the above equation can be written as

$$n_{cr} (cm^{-3}) = \frac{1.1 \times 10^{21}}{\lambda_{\mu m}^2} \quad (2.18)$$

For the relativistic intensity lasers considered in this thesis, relativistic correction is needed. This gives expression for relativistic critical density is $n_{cr}|_{relativistic} = \gamma_{osc} n_{cr}$. Here γ_{osc} is the Lorentz factor due to the oscillatory motion of electrons in presence of laser as discussed in the earlier section.

Now, for the case of inhomogeneous plasma which may be more relevant for this thesis, analytical solution can be obtained with WKB method. Equivalent result can be obtained from simple energy flux conservation argument. Since the group velocity of the light $(V_g/c = \sqrt{1 - \omega_{pe}^2/\omega^2} = \sqrt{\epsilon})$ decreases with increase in

the plasma density, we see that the laser electric field must increase as it approaches the critical density surface from the low density region. This can be shown as

$$\frac{V_g |E_{Laser}(z)|^2}{8\pi} = \frac{cE_0^2}{8\pi} \Rightarrow |E_{Laser}(z)| = \frac{E_0}{\epsilon^{1/4}} \quad (2.19)$$

Here E_0 and $E_{Laser}(z)$ are the laser electric fields in vacuum and inhomogeneous plasma respectively. Finally it should be pointed out that since wave propagation vector becomes imaginary beyond critical density surface, the electric field dies down exponentially in the overcritical region. Exact analytical solution for linear density profile can be expressed in terms of Airy functions [Kruer, 2003]

Laser propagation through pre-formed plasma can also be subjected to various parametric instabilities such as Stimulated Raman Scattering (SRS), Stimulated Brillouin Scattering (SBS), ' $2\omega_{pe}$ ' instability, laser beam filamentation, laser self focussing etc. These instabilities are discussed in great detail by William Kruer [Kruer, 2003]. Out of these instabilities, probably the most important ones in the context of short pulse laser with relativistic intensity are laser filamentation and self-focussing. The essential physics of these two instabilities can be summarized by the following schematic figure.

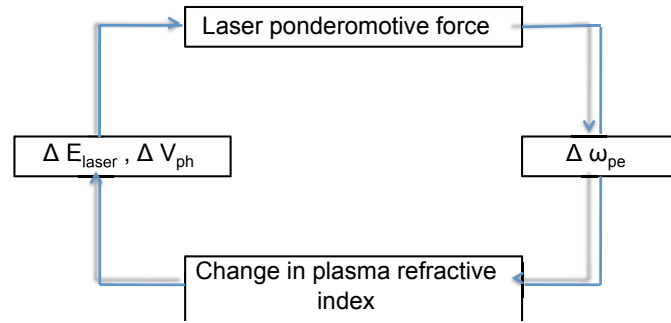


Figure 2.1: Schematic for laser filamentation and self-focusing instability .

Here change in plasma frequency ω_{pe} can be introduced due to the various factors such as transverse density profile of the pre-formed plasma, radial intensity profile of the laser beam, small perturbations in the directions transverse to the laser propagation. On the other hand, change in the local phase velocity of the light

will lead to either beam filamentation or self-focusing. Recent PIC simulations [Kemp et al., 2010, MacPhee et al., 2010] of laser interaction with cone targets which are filled with pre-formed plasma demonstrate laser filaments (see Figure 2.2). As can be seen from these simulations, filamentation and self-focusing can increase the local intensity of laser inside pre-formed plasma. Hence, these effects will have implications on the generation of relativistic electrons in the pre-formed plasma.

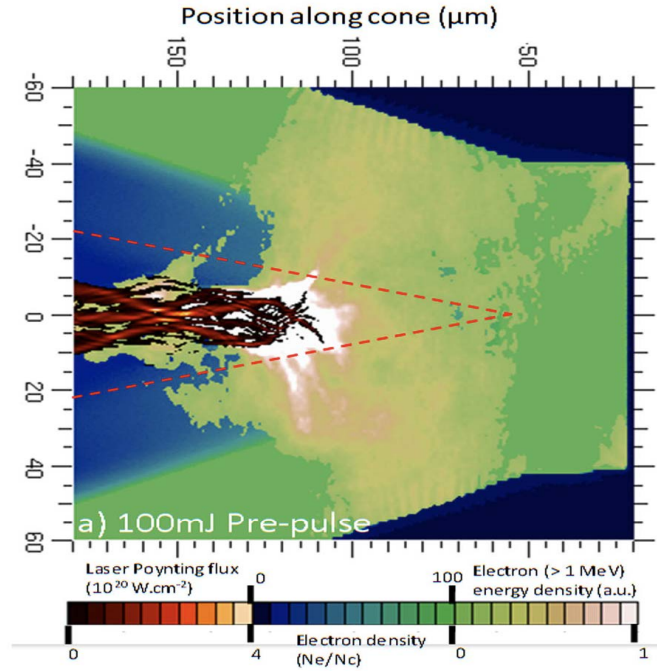


Figure 2.2: PIC simulations of laser filamentation while propagating through pre-formed plasma. [MacPhee et al., 2010]

2.3 Laser absorption mechanisms and fast electrons generation

The topic of laser absorption and fast electrons generation is extensively studied both theoretically and experimentally. Since electron while oscillating in an infinite electromagnetic radiation gains exactly same amount of energy in one half cycle as it loses in the other half cycle, the net energy gain from an

electromagnetic radiation is always zero [Woodward and Lawson, 1948]. Therefore in order for the electron to gain energy from laser, this symmetry of oscillation must be broken. This is the essence of all the laser absorption mechanisms. This also means that the generated electron spectrum is closely associated type of laser absorption mechanism.

In the context of relativistic intensity lasers, two widely used scalings to predict the fast electrons energy spectrum are experimentally determined ‘Beg scaling’ [Beg et al., 1997] and numerically found ‘Wilks scaling’ or ‘ponderomotive scaling’ [Wilks et al., 1992]. Both these scalings attempt to characterize the fast electrons energy distribution function with a ‘slope temperature’ T_{hot} by assuming Maxwellian distribution. T_{hot} in ‘Beg scaling’ depends upon $[I_L \lambda_L^2]^{1/3}$ whereas the ‘Wilks scaling’ predicts it as $[I_L \lambda_L^2]^{1/2}$ where I_L and λ_L are laser intensity and wavelength respectively. The energy scaling of fast electrons with laser intensity is still a topic of active research and this thesis makes an attempt to contribute to this on going discussion.

Typically, collisional absorption and resonance absorption are the dominant heating mechanisms for the low intensity ($< 10^{17}$) W/cm², long pulse (hydrodynamic time scales) lasers [Kruer, 2003]. In collisional absorption, the electron-ion collisions break the symmetry of the electrons oscillation, thereby resulting in laser absorption. In high power short pulse lasers, plasma becomes almost collisionless due the high temperatures and large oscillation velocity (compared to the thermal velocity) of electrons. Generally collisional absorption is considered to play important role up to the intensities 10^{15} W/cm². The resonance absorption occurs when p-polarized light is incident obliquely on the plasma with its electric field component parallel to the density gradient. This oscillating component of electric field excites electrostatic plasma waves (Langmuir waves) which mostly travel down the density gradient. These waves eventually are damped either collisionally or through Landau damping, thereby giving energy to the electrons. The generated electrons are typically ‘superthermal’ with temperature which scales as $[I_L \lambda_L^2]^{1/3}$, curiously similar to the experimentally measured Beg scaling.

In case of sharp density gradient overcritical plasma, the mechanism called

‘vacuum heating’ or ‘Brunel absorption’ [Brunel, 1987] explains collisionless absorption of high intensity laser incident. In this case, the component of electric field of obliquely incident laser, drags and accelerates thermal electrons into vacuum. These electrons eventually enter overcritical plasma on the reversal of polarity of accelerating electric field. Since the energy of accelerated electrons is proportional to the component of laser electric field normal to the surface, the T_{hot} for this mechanism scales with $[I_L \lambda_L^2]^{1/2}$. Similar to vacuum heating, reflection of the electron inside the electrostatic sheath in front of overcritical plasma can break the symmetric of oscillation for an electron in a laser field. This may result in laser absorption. Based on this effect, heating mechanisms such as ‘anomalous skin effect’ [Gamaliy and Tikhonchuk, 1988, Weibel, 1967] and ‘sheath inverse-bremsstrahlung’ [Catto and More, 1977] are proposed.

Another important absorption mechanism in the context of short pulse laser matter interaction with steep density gradients is ‘ $J \times B$ heating’ [Kruer and Estabrook, 1985]. Here, the oscillating component of the relativistic ponderomotive force plays a role similar to the component of laser electric field normal to the surface in case of resonance absorption and vacuum heating. As we have seen earlier in this chapter, since this ponderomotive force oscillates at twice the laser frequency, the fast electrons are accelerated and pushed into the target with characteristic ‘ 2ω ’ bunches [Mishra et al., 2009]. This mechanism leads to ‘ponderomotive scaling’ i.e. $[I_L \lambda_L^2]^{1/2}$ for T_{hot} which is confirmed by PIC simulations [Wilks et al., 1992].

Thus we see at that the applicability of these absorption mechanisms in laser-solid interactions may depend upon various factors such laser intensity, pre-formed plasma density scale-length, target material etc. Not so surprisingly the distribution function of the generated fast electrons in such interactions shows distinct departure from the ‘ideal’ Maxwellian distribution.

2.4 Electron beam transport through plasma

The topic of transport of fast electrons through plasma in relativistic intensity laser matter interaction is very important for the fast ignition studies. Such interactions generate relativistic electron beams carrying very high currents. The currents can be estimated for typical laser parameters. For a given laser intensity I_{Laser} and conversion efficiency α of laser to fast electrons we can estimate fast electron current density J_{fast} as

$$J_{fast} [A/cm^2] = \frac{\alpha I_L [W/cm^2]}{T_{hot} [eV]} \quad (2.20)$$

For the laser intensity of 10^{19} W/cm² and $T_{hot} \sim 1$ MeV (ponderomotive scaling), taking conversion efficiency of 10% , we can estimate the fast electrons current density as $\sim 10^{12}$ A/cm². Assuming that this electron beam is approximately cylindrical with a radius of $10 \mu m$, the total fast electrons current turns out to be 3 MA. Now let us compare this current with the ‘Alfven current limit’ [Alfvén, 1939, Dodin and Fisch, 2006]. The ‘Alfven current’ I_A is the maximum current than can be transported through a medium due to the self-pinching effect of beam magnetic field. It’s expression is given by

$$I_A = \frac{mc^3}{e} \gamma V_z$$

$$I_A|_{electron} [kA] = 17 \gamma V_z \quad (2.21)$$

Here V_z is the normalized velocity of the particle in beam. For a electron beam of average energy of 1 MeV, this current limit is ≈ 50 kA. Thus the total current in the relativistic electron beam generated in typical short pulse laser matter interaction experiment exceeds the ‘Alfven current limit’ by a factor of 600 !! This anomaly can be resolved by considering that such high current must be compensated by a backward current from background plasma so that the net current is close to zero i.e. $J_{net} = J_{fast} + J_{plasma} \approx 0$ [Bell et al., 1997]. This current is generally referred as ‘return current’.

Naturally such return current would set up a resistive electric field due to collision of electrons in the return current with the background plasma ions. This resistive electric field for a background plasma with resistivity η can be estimated using Ohm's law as

$$E = \eta J_{plasma} \quad (2.22)$$

Based on work by Lee and More [Lee and More, 1984], for a solid density of aluminum target at 200 eV temperature and mean ionization state 10, we can apply Spitzer resistivity formula $\left(\eta = 5.22 \times 10^{-3} Z \log \Lambda T_{plasma}^{-3/2} \Omega - cm\right)$. Taking $\log \Lambda = 2$ we get $\eta = 3.69 \times 10^{-5} \Omega - cm$. Therefore, for current density of 10^{12} A/cm², the resistive electric field is $\approx 3.7 \times 10^{-3}$ MV/ μm . Correspondingly the stopping distance for 1 MeV electron is $\sim 270 \mu m$ which is considerably smaller than the classical stopping distance of electron in the solid. Although these simple estimates are far from exact, they demonstrate that the dynamics of such high current density fast electrons beam is significantly altered when it propagates through plasma. The dynamics of these fast electrons is also affected by the magnetic fields generated by resistive electric fields. Taking curl of Eq. 2.22 and noting that $J_{plasma} \approx -J_{fast}$, we can write the equation for resistive magnetic fields as

$$\frac{1}{c} \frac{\partial \vec{B}}{\partial t} \simeq \nabla \eta \times \vec{J}_{fast} + \eta \nabla \times \vec{J}_{fast} \quad (2.23)$$

This means that magnetic fields can be generated either in case of non-uniform current density or if there is a resistivity gradient in the path of fast electrons beam. For example, such fields can be excited at the interface of two different materials due to gradient in resistivity [Bell et al., 1998].

We see that the fast electrons transport through plasma is strongly affected by the strong electric and magnetic fields produced by the interplay of forward of fast electrons and backward current of background plasma. The physics of transport is further complicated by the fact that this set up of counter-propagating currents is unstable to various electrostatic and electromagnetic instabilities. In particular, the weibel like electromagnetic instability [Califano et al., 1997, Weibel,

1959] which may cause the filamentation of fast electron beam can significantly influence the transport.

Thus we see that the relativistic fast electrons generation and transport is rich topic in physics with very interesting phenomena. After reviewing this basic essential theory of the subject, we now begin our exploration of influence of pre-formed plasma on these fast electrons when the laser interacts with the solid target.

Chapter 3

Fast electron generation in the presence of pre-formed plasma

As we discussed in Chapter 1, the pre-formed plasma density scale-length could be as high as 15-20 μm (in planar targets) for a typical energy contrast of 10^{-5} between the pre-pulse and energetic main pulses of energies 10-100 kJ. Even in the case of a laser system with a high energy contrast ratio ($\sim 10^{-8}$), considerable plasma can be expected to build up in front of a dense target due to plasma expansion for a relatively long pulse (~ 20 ps), high intensity, high power lasers, especially in the fast ignition relevant experiments. Therefore, the interaction of the short pulse laser with pre-formed plasma is inevitable in laser-solid interaction experiments, particularly with $1\mu m$ lasers.

Typically, laser plasma interaction (LPI) generated fast electrons are characterized by the slope temperature, T_{hot} , of their energy spectrum. The two most widely used scaling for the fast electrons mean energies (T_{hot}) are the experimentally determined Begs scaling [Beg et al., 1997] and Wilks numerically modeled ponderomotive scaling [Wilks et al., 1992]. These scalings do not address the dependence of T_{hot} on a finite scale-length pre-formed plasma in front of the target. However, as discussed in chapter 1, the recent experiments and numerical modeling suggest that the presence of pre-formed plasma can significantly affect the fast electron energy distribution. In general, these studies have reported an increase in the fast electrons mean energy with increasing pre-formed plasma scale-length.

However, the physics of such increase in the fast electron energy with increasing pre-formed plasma is still not well-understood.

In this chapter, we discuss the fast electron generation in the presence of pre-formed plasma in laser-matter interaction in the intensity range of 10^{19} - 10^{21} W/cm² in a 1-dimensional slab approximation. Results of numerical simulations with PIC code LSP are presented here. Three different pre-formed plasma density scale-lengths of 1 μm , 5 μm and 15 μm are considered. The choice of simplified 1-D approximation, because it is computationally cheap, allows us to simulate the laser plasma interaction over a wide range of pre-formed plasma scale-lengths and laser intensities. Consistent with the earlier reported work, it is found that both the mean and the maximum energy of the generated fast electrons increase with an increase in the pre-formed plasma scale-length (in the range 1-15 μm).

The simulations are performed with both mobile and immobile ions assumption. In the majority of our simulations, the ions are considered to be immobile in order to keep the interaction independent of solid target material. The effect of ion mobility and ponderomotive steepening of plasma density profile [Kemp et al., 2009] is studied by performing separate simulations for the case of fully ionized aluminum. The multi-dimensional effects of laser plasma interaction like laser self-focusing [Kelley, 1965, Sun et al., 1987] and filamentation [Max et al., 1974] may play a role in experiments. However, these effects are neglected in the present work for simplicity.

3.1 PIC modeling with immobile ions

The simulations are performed with the PIC code, Large Scale Plasma (LSP), used in 1D3V phase-space. LSP, being an implicit PIC code, allows the use of the grid resolution greater than the Debye length without causing excess numerical heating. This feature makes it suitable for simulating laser-solid interactions at relativistic intensities. For example, the Debye length for plasma at a density of 10^{23} cm⁻³ and 5 keV electrons temperature is approximately 1.6×10^{-3} μm . LSP relaxes the stringent computational requirement of resolving such small

spatial scales. A spatial resolution of 80 cells per laser wavelength ($= 1 \mu m$) with 300 particles per cell is used in the simulations. The cell size, $\Delta_z = 1.25 \times 10^{-2} \mu m$, ensures that the collisionless skin depth and lowest pre-plasma scale length ($1 \mu m$) are well resolved. The time step $c\Delta t = 10^{-3} \mu m$ is chosen to satisfy the Courant stability criterion [Welch et al., 2001]. The initial plasma density profile is taken as [Sherlock, 2009].

$$n_e(z) = \frac{Z_i n_{solid}}{1 + \exp [1 + 2(z - z_0)/L_p]} \quad (3.1)$$

where L_p denotes pre-formed plasma scale length, Z_i is the ion charge state and n_{solid} is the solid ion density. Fully ionized aluminum plasma with initial temperature of 5 keV is used in the simulations. The selection of aluminum would only affect mobile ion simulation results through its ion inertia. Of course, the implicit assumption here is that the slow ion motion can be neglected on the time scales of fast motion of electrons in the laser field and ion motion would affect the LPI only through the modification of pre-formed plasma profile. The linearly polarized laser enters the simulation box from the left boundary (figure 3.1) with the laser pulse reaching maximum intensity in 10 laser cycles (i.e. 33 fs). The simulations are run with three different laser intensities of 10^{19} W/cm^2 , 10^{20} W/cm^2 and 10^{21} W/cm^2 . The direction of laser propagation is defined as Z-direction, whereas the laser electric and magnetic fields are pointed in the X and Y direction respectively. The fast electron energy spectrum is obtained by analyzing the electrons behind the relativistic critical density surface (inside the counting box B as shown by dotted lines in figure 3.1). Figure 3.1(b) shows the temporal variation of Poynting flux through plane AA for the case of $I=10^{20} \text{ W/cm}^2$. Quasi-steady state of the simulation is defined as the time when laser net forward energy flux becomes approximately constant and equal to the particle energy flux entering the solid target. The estimate of the fast electrons mean energy based on electron distribution functions is obtained when this quasi-steady state is reached. For example, in figure 3.1(b), quasi-steady state is reached approximately after 400 fs. Fast electron refluxing from the back of the target is avoided by choosing longer target

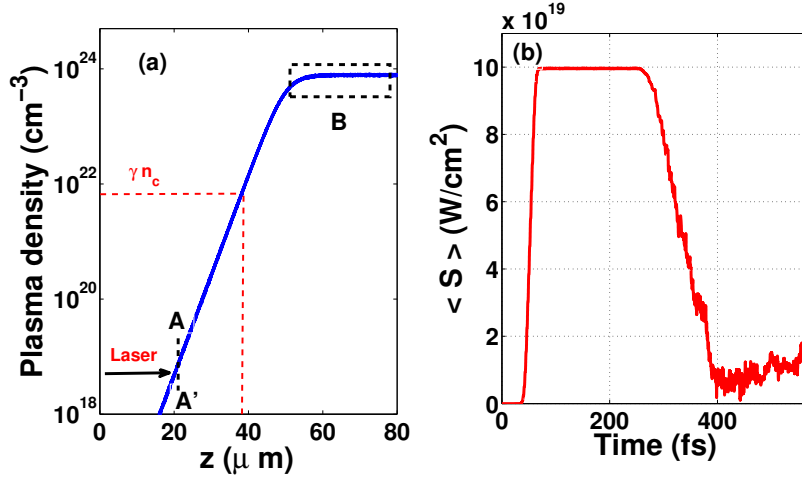


Figure 3.1: Schematic of simulation set-up. (a) The linearly polarized laser enters the simulation box from the left boundary and travels in +Z direction. The fast electrons generated by laser plasma interaction are counted inside the solid in box B for the analysis of electron energy distribution. (b) The temporal variation of laser forward energy flux through plain AA is shown.

dimensions. Therefore, results presented here are valid under the thick target approximation with no refluxing of electrons from a foil's rear surface into the LPI region. Such electron refluxing could significantly modify these simulations [Chen and Wilks, 2005].

One issue that is critically important in high intensity laser-matter interaction is to characterize correctly the fast electrons energy spectrum. In general, the most important quantity of interest is the mean energy (E_{mean}) of generated fast electrons going into the target. Typically this quantity is determined by fitting the electron distribution function, $f(E)$ (shown in figure 3.2(a)) by a function of the form $A_0 \exp(-E/T_{\text{hot}})$ where T_{hot} is called slope temperature. The electron distribution function $f(E)$ is normalized as:

$$n = \int_0^{\infty} f(E) dE \quad (3.2)$$

where, n is the electron density and E is the kinetic energy of an electron. But this direct correlation between E_{mean} and T_{hot} breaks down when the electron energy

spectrum is non-Maxwellian, which is usually the case with the high intensity laser-matter interactions. Therefore, the mean energy of fast electrons obtained from this method is very sensitive to the energy range chosen to fit the spectrum, especially in the low energy part of the spectrum [Sherlock, 2009]. The more meaningful estimate of the fast electron mean energy, especially for fast ignition [Tabak et al., 1994] studies, can be made based on the electron energy flux distribution function or heat flux, $w(E)$ defined in the following way:

$$q(E) = \int_0^E w(E)dE = \int_0^E f(E)EV_z dE \quad (3.3)$$

where $q(E)$ is the heat flux carried along the laser propagation direction by the electrons with energies less than E , and V_z is the electron velocity in the laser propagation direction. Thus, the total heat flux q_T carried by the electrons inside the target is given by

$$q_T = \int_0^\infty w(E)dE = \int_0^\infty f(E)EV_z dE \quad (3.4)$$

Now, we define the mean energy E_{mean} of the fast electrons spectrum as energy at which half of the total electron heat flux ($0.5q_T$) is captured. Figure 3.2(b) illustrates the method of calculating the mean energy in this work. This method gives us a direct quantitative estimate of the energy at which the incident laser energy is converted into the fast electrons energy without the introduction of any arbitrary lower energy cutoff, which was used in Ref. [Sherlock, 2009].

The fast electron energy spectra obtained for the three pre-formed plasma scale-lengths ($L_p = 1, 5, \text{ and } 15 \mu m$) at three laser intensities ($I = 10^{19}, 10^{20}, 10^{21} \text{ W/cm}^2$) are analyzed by the above-mentioned method. Figure 3.3 (a) shows the fast electron energy spectra at the laser intensity of 10^{20} W/cm^2 . The dependence of the mean electron energy on laser intensity and pre-formed plasma scale-length is plotted in figure 3.3(b). It can be seen that the longer scale-length pre-formed plasma results in the higher mean energy of fast electrons, in agreement with earlier published experimental and numerical work. For the long pre-formed plasma cases

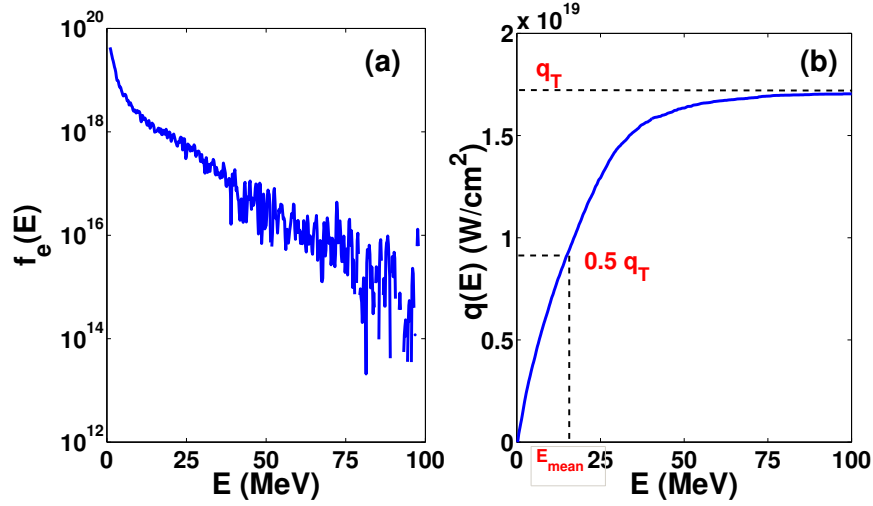


Figure 3.2: (a) Electron energy distribution inside the target for laser intensity of 10^{20} W/cm² and 15 μ m pre-plasma scale-length (b) Cumulative heat flux carried by the electrons inside the target.

(viz 5 and 15 μ m), the E_{mean} obtained is higher than the laser ponderomotive energy, E_p for the corresponding laser intensity. In addition, we also observe that the maximum energy of fast electrons in the spectrum (E_{max}) increases with an increase in the pre-formed plasma scale-length. For example, for the laser intensity of 10^{20} W/cm², the mean energies for 1, 5 and 15 μ m cases are approximately 3.1 MeV, 6.3 MeV and 14 MeV respectively, whereas the ponderomotive energy at this intensity is 3.8 MeV. The corresponding maximum energies for these scale-lengths are 25 MeV, 75 MeV and 100 MeV respectively.

Finally, we performed the chi-square minimum fitting on the mean energies obtained for the various intensities and pre-formed plasma scale-lengths with a fitting function of the form , where I_L and L_p are the laser intensity normalized by 1.37×10^{18} W/cm² and pre-formed plasma scale-length in μ m respectively. This fitting gives E_{mean} as

$$E_{\text{mean}}(\text{MeV}) = (0.72 \pm 0.13) I_L^{(0.36 \pm 0.02)} L_p^{0.5 \pm 0.06} \quad (3.5)$$

Note that above fitting is obtained for the laser intensity range of $10^{19} - 10^{21}$

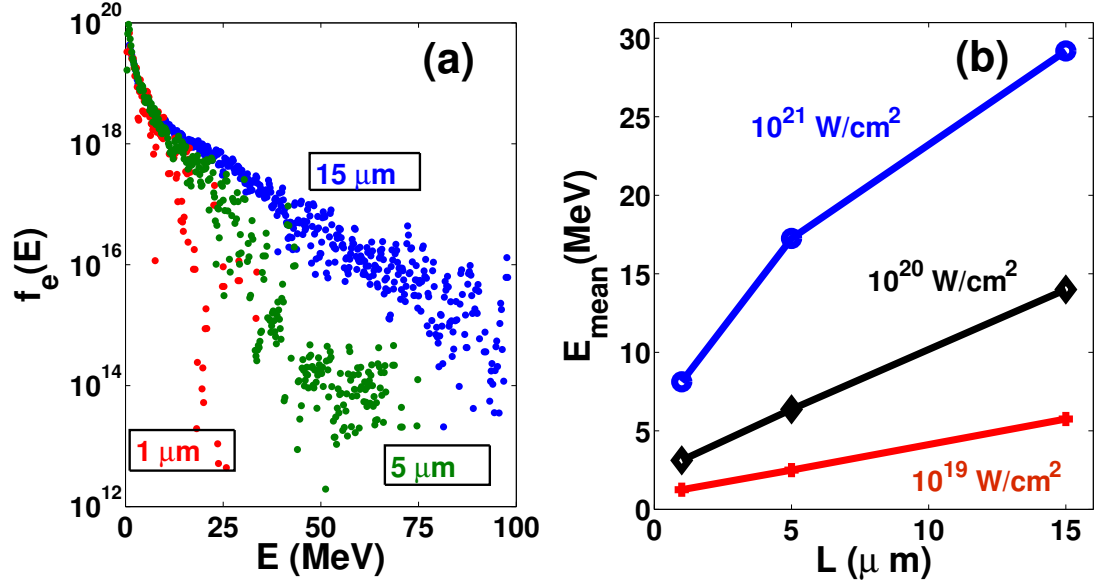


Figure 3.3: (a) Electron energy distribution inside the target for three pre-formed plasma scale-lengths for a laser intensity of $10^{20}\ \text{W/cm}^2$. (b) The mean energy of electrons obtained by the method described in figure 3.2(b). The increase in both the mean and maximum energy with increasing pre-formed plasma scale-lengths is evident from these plots.

W/cm^2 and pre-formed plasma scale-length range of $1\text{--}15\ \mu\text{m}$. Thus, we find that both the mean and the maximum energies of the generated fast electrons increase with an increase in the pre-formed plasma scale-length. In order to understand the underlying physics of the above-mentioned results, we have analyzed the dynamics of the electrons as the laser starts interacting with the pre-formed plasma. In the next section, we discuss the dynamics in detail.

3.2 Dynamics of electrons in the pre-formed plasma

As described above, the mean electrons energy and spectra are affected by the pre-formed plasma scale-lengths. Now, the key question is what is the mechanism of the plasma electrons heating which leads to such varying spectra with pre-formed plasma scale-lengths? In this section, we will address this question. The essential feature of electron heating by an EM wave is the phase randomization

of electrons in an oscillating field of the wave. This is due to the fact that a single electron oscillating coherently with the electric field of a plane wave gains zero cycle averaged energy since the electron energy gain in one half cycle is exactly equal to the energy loss in the next half cycle. This is generally referred to as Woodward-Lawson theorem [Woodward and Lawson, 1948]. The various causes of this breaking of phase coherence in laser plasma interaction results in electron heating or laser absorption mechanism as discussed in Chapter 2. In this section , we investigate the electron heating process by analyzing the electron phase-space (P_z vs z) dynamics at various stages of the interaction. Figure 3.4 describes the dynamics of laser interaction with pre-formed plasma during the initial stages for the case of laser intensity of 10^{20} W/cm² and pre-formed plasma scale length of $5 \mu m$. The phase space density, $D(z, P_z)$ shown in figure 3.4 (a), (c) and (e) gives a number proportional to the number of electrons found between z and $z+dz$ having longitudinal momentum in the range P_z and P_z+dP_z . The normalized electrostatic potential due to longitudinal electric field E_z is also shown in the red curve. The electron momentum is plotted in the usual dimensionless units of $\gamma\beta$. Figures 3.4 (b), (d), and (f) are the electron (red line), ion (blue line) densities and the laser electric field, E_x corresponding to the times shown in figure (a), (c), and (e) respectively. In very early stages of laser propagation through under-dense pre-formed plasma (refer figure 3.4(a) and 3.4(b)), all the electrons are swept away in the forward direction (+Z-direction) by the laser ponderomotive force, leaving behind immobile ions. This forward electron acceleration by the ponderomotive force is evident from 2ω electron oscillations. The electrostatic potential due to charge separation in the under-dense plasma tries to pull the electrons in the backward direction. As the laser propagates further towards a critical density surface (refer figure 3.4(c) and 3.4(d)), the electrons experience stronger backward pull due to increasing electrostatic potential. Negative values of momentum in figure 3.4(c) illustrate the backward movement of some of the electrons. Now, the reversal of longitudinal electric field polarity (in the Z direction) in response to this backward movement of electrons can be seen from the potential curve in this figure. Finally, we observe the strong phase-space mixing when part of the

incident light is reflected back from the relativistic critical density ($\gamma_{osc}n_c$) surface which is present at $48 \mu m$ for this simulation (refer figure 3.4(e) and 3.4(f)). Here, γ_{osc} for laser vector potential a_0 is defined as $\gamma_{osc} = \sqrt{1 + a_0^2/2}$. The phase-space mixing occurs in the region (between $30 \mu m$ and $50 \mu m$) where we have two counter propagating EM waves (incident and reflected laser light). The increase in the electron energy with the disappearance of distinct 2ω oscillations in this region demonstrates the stochastic electron heating [Bourdier et al., 2007, Sheng et al., 2004] by these two counter-propagating waves. We also observe strong non-linear electrostatic plasma waves produced by the laser ponderomotive force, travelling pre-dominantly down the density gradient (against the direction of incident laser propagation, i.e. Z direction) as in the resonance absorption. But the contribution of these waves to electron heating via wave-particle interactions like Landau damping is found to be insignificant. The peak value of electrostatic potential of these plasma waves is much smaller than the actual energy gain by the electrons seen in the simulations. Therefore, for the laser intensities simulated in this work, we find that the stochastic heating by counter-propagating EM waves is the dominant mechanism.

As the electrons heating continues, the stochastic motion of electrons in counter propagating EM waves leads to the mixing of phase-space fluid. This results in homogenization of phase-space density in the region of mixing. This physical picture can be seen in the later time phase-space density plots shown in figure 3.5. The colors in these plots show the local phase-space density. Also, this representation of phase-space density indicates how the electrons energy spectrum varies with spatial co-ordinates; e.g. the flow of phase-space fluid. Thus, from figure 3.5 we can infer that the very high-energy tail (shown by blue color) of the electron distribution inside the target is essentially due to the electrons in the low-density region of the pre-formed plasma. Here, we would like to emphasize the fact that this phase-space fluid trajectory should not be mistaken as the trajectory of an individual electron in that region of phase-space. This is especially true in the phase-space mixing region.

The electron heating near the relativistic critical density surface results in

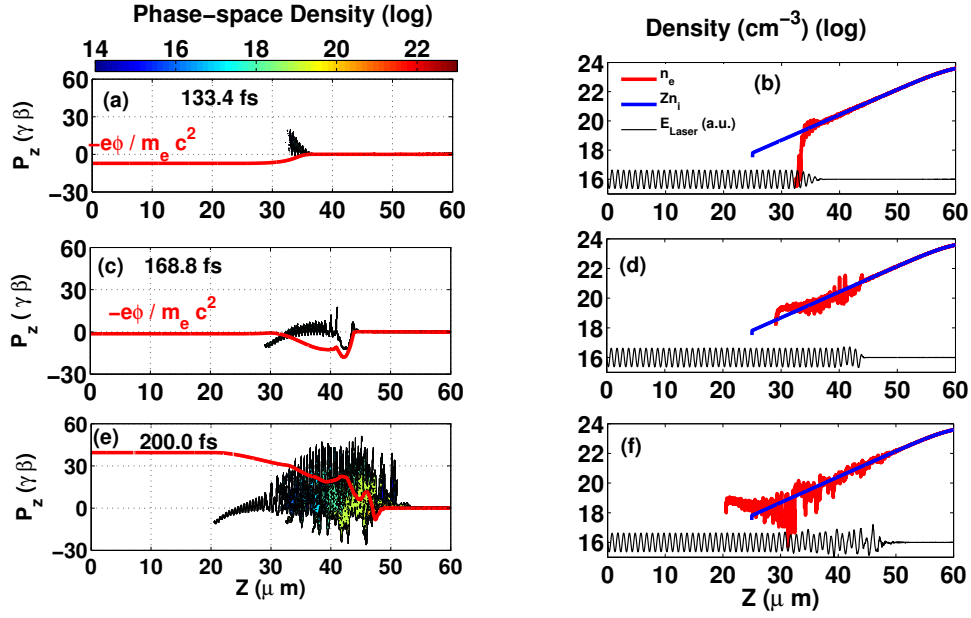


Figure 3.4: Laser interaction with pre-formed plasma during initial stages of laser propagation through under-dense plasma.

an increase in electron pressure ($n_e T_e$) in the region of laser absorption. The pressure gradient causes the heated plasma expansion from the absorption region. The electrostatic potential well (solid red line in figure 3.5) self-consistently appears in response to the plasma electrons expansion from this region. In other words, the plasma electrons' heating causes the setting up of this longitudinal electrostatic potential well to maintain quasi-neutrality. The progressive increase in the maximum value of potential (from figure 3.5 (a) to (c)) and corresponding decrease in the electrons escaping to the lower density side (from 0 to $30 \mu m$, in figure 3.5) demonstrates how plasma potential changes in order to maintain quasi-neutrality. It should be noted that this potential also brings the cold, fresh electrons from the solid target into the interaction region. The cold electrons finally enter the target as heated electrons. This explains how the quasi-steady state is achieved in these simulations (typically in 200 to 400 fs depending upon the pre-formed plasma scale-length). With this picture of the pre-formed plasma electrons heating in mind, we now try to investigate the differences in the electron energy spectra inside the target for different pre-formed plasma scale-lengths by comparing the

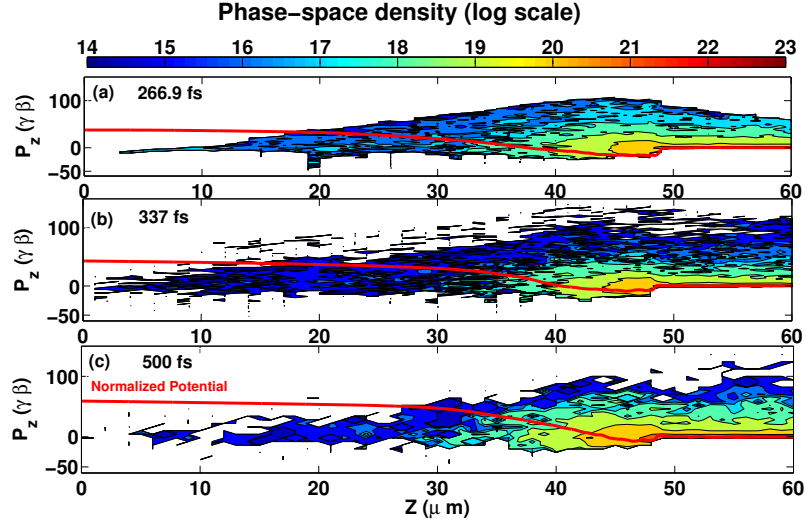


Figure 3.5: Phase-space density and electrostatic potential (solid red line) evolution as laser starts heating the pre-formed plasma. The increase in the maximum value of the potential and corresponding decrease in the electron density escaping toward low-density side demonstrates how plasma confines these electrons.

quasi-steady state phase-space density plots of different scale-lengths (5 and 15 μm) for the same laser intensity of 10^{20} W/cm² (see figure 3.6). Note that the relativistic critical density surface is defined as $Z = 0$ in these figures. Clearly, we see an extension of the phase mixing region in the case of a shallower density profile ($L_p = 15 \mu m$) with wider potential well due to the reduced longitudinal electric field. Here, the electric field is weakened because of the long scale-length of the pre-formed plasma. The increase in electron energy for the same phase-space density (shown by the same colors found in figure 3.6(a) and 3.6(b)) indicates the increase in mean energy in the case of long scale-length pre-formed plasma compared to the short scale-length pre-formed plasma. Also, the maximum energy of electrons seen inside the target is greater for the 15 μm scale-length case. Thus, these observations are consistent with the results reported in section II. From this we conclude that the extension of the phase-space mixing region in the presence of a wider potential well leads to higher mean and maximum fast electron energies for the case of long scale pre-formed plasma. In addition, we observe that the mean energies for these two cases are higher than the ponderomotive energy E_p at the given laser intensity (refer figure 3.3). For example, for laser intensity

10^{20} W/cm², E_p is 3.8 MeV; whereas mean energies for 5 μm and 15 μm are 6.37 MeV and 17.25 MeV respectively. These results indicate that the electron heating process is strongly influenced by this longitudinal electrostatic potential well. In order to investigate the exact physics behind this increase in electron energies in the presence of long scale pre-plasma with mean energies greater than ponderomotive energy, we performed a separate set of simulations with counter propagating EM waves with and without the electrostatic potential well. Note that the counter propagating EM wave and electrostatic potential well associated with the expansion of heated plasma electrons are found to be essential features of the laser-plasma interaction for all the pre-formed plasma scale-lengths. The width and the depth of this well are decided by various factors such as plasma heating, pre-formed plasma scale-length, ion mobility (this will be demonstrated in section V), etc. The numerical results and physics of electron heating in the presence of a potential well are discussed in the next section.

3.3 Electron heating due to synergetic effects of EM radiation and electrostatic potential well

The phase-space dynamics in counter propagating EM waves with or without the presence of an electrostatic potential well can be understood by first analyzing the motion of a single electron in such a field. We have studied such motion by numerically solving 1D3V electron equation of motion with the standard Boris algorithm [Birdsall and Langdon, 1985]. Figure 3.7 shows the phase-space trajectories of a single electron under various conditions. The intensity of both the counter propagating linearly polarized EM waves is taken as 10^{20} W/cm². Figure 3.7(a) shows the trajectory of the electron in the absence of a longitudinal electric field. The characteristic feature of electron motion consisting of trapping (shrinking of phase-space area, i.e. adiabatic invariant) and de-trapping of the electron is clearly evident from this figure. The maximum normalized longitudinal momentum seen is around 30. Next, in figure 3.7(b), we introduce a constant longitudinal electric field (i.e. linearly increasing normalized potential represented by blue line)

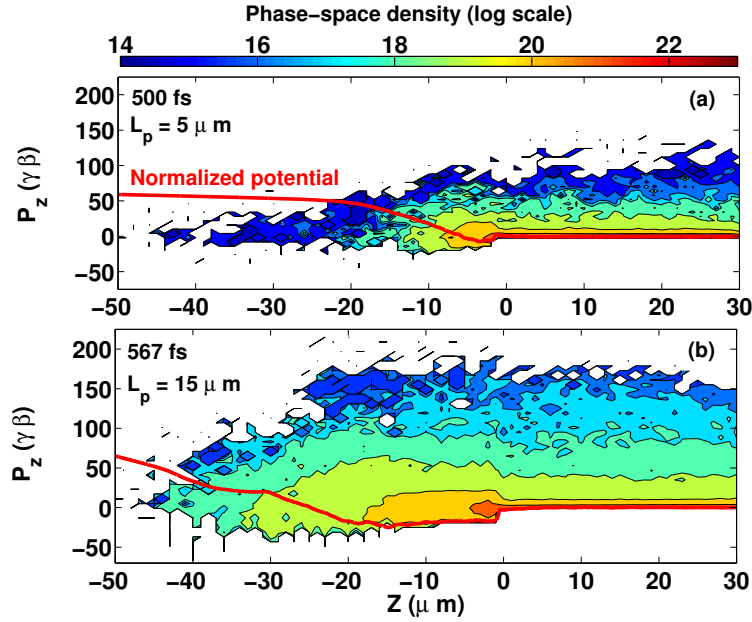


Figure 3.6: Comparison of phase space plots for (a) $5 \mu\text{m}$ and (b) $15 \mu\text{m}$ pre-formed plasma scale lengths (Laser intensity = 10^{20} W/cm^2). Note the extension of phase-space mixing region (0 to $-45 \mu\text{m}$) for the case of $15 \mu\text{m}$ pre-formed plasma with higher energies compared to $5 \mu\text{m}$ pre-plasma. Also, the electrostatic potential well developed in pre-formed plasma due to the electron heating is wider for long scale-length pre-formed plasma.

in addition to these counter propagating EM waves. Because of the constant electric field, which pushes the electron continuously in $+Z$ direction in this case, the phase-slippage of electron with respect to the forward propagating wave is reduced and therefore the electron starts moving with the forward propagating ($+Z$) EM wave. We define this process as electron locking with the forward wave. Note that the energy gain of the electron is much greater than the electrostatic potential. Thus, the longitudinal electric field helps in reducing the phase-slippage of an electron with respect to one of the EM waves, thereby causing the non-linear increase in energy of the electron due to locking with that wave. In the next three cases (figure 3.7(c) to (e)), we analyze electron motion for different initial positions (at $t = 0$) in a quadratic electrostatic potential well (shown by blue line). These cases mimic the situations in the actual simulations described in the previous section. In each of these cases the electron starts from rest with the initial positions ($Z =$

0 μm , -20 μm , -30 μm for Fig. (c), (d) and (e) respectively). From figure 3.7(c) to 7(e), we see that the electron, once de-trapped, oscillates in the potential well by alternately getting locked with the forward and backward going EM wave. During this process it also gains energy continuously, thereby climbing up the potential during each cycle of forward and backward motion. This feature can be seen from figure 3.7(e) where the electron starts from $Z = -30 \mu m$, but after one cycle of oscillation climbs up in the potential at $Z = -35 \mu m$. Also, note the increase in the maximum energy of the electron, as it starts from a region of stronger electric field. The stronger electric field acts as a moderator in reducing phase-slip of the electron with respect to the EM wave, thereby causing higher acceleration due to increased locking distance with either wave. This is consistent with the results in actual simulations where the maximum energy component of the spectrum inside the target comes from the electrons accelerated from the under-dense plasma which is also a region of higher electrostatic potential (refer figure 3.6). Also, large pre-formed plasma allows longer acceleration length to these electrons locked with the forward wave, thereby resulting in an increase in the maximum energy. Keeping the single particle dynamics in mind, it is now easy to interpret the results of PIC simulations performed to explain plasma heating in two counter propagating EM waves with and without electrostatic potential well.

The numerical set up and results demonstrating plasma heating due to counter propagating EM waves in a potential well (at steady state) are shown in figure 3.8. The two linearly polarized EM waves with equal intensity of 10^{20} W/cm² enter the simulation box from the left and right boundaries (figure 3.8(a)). The plasma density in these simulations is 10^{16} cm⁻³. This extremely low value of plasma density ensures that the self-consistently excited longitudinal electric fields (including plasma waves) are negligible and plasma heating is entirely due to the counter propagating EM waves and externally imposed electrostatic potential well. As can be seen from figure 3.8(a), simulations are run for two different potentials (potential A (red curve) and potential B (blue curve)). In addition, we also performed a simulation without the potential well for comparison. The phase-space densities for the cases without potential (figure 3.8(b)) and with potential

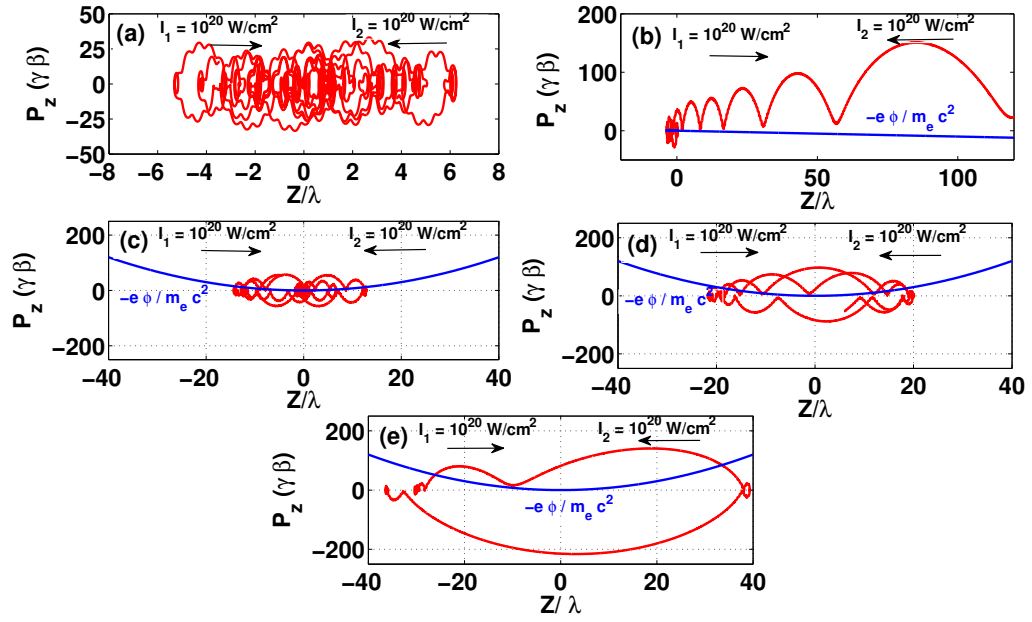


Figure 3.7: Single electron phase-space trajectories with counter propagating EM waves and longitudinal electric field. (a) Stochastic electron motion without longitudinal electric field. (b) The electron motion in the presence of constant longitudinal electric field. (c), (d), (e) The electron dynamics in the presence of quadratic potential well (shown by blue line) for the electron initial positions of 0, -20 and -30 respectively. The electron, starting higher up (for example figure (e)) in the potential, gains more energy due to locking with either of the waves.

A (figure 3.8(c)) show the increase in electron energies in the presence of the potential well. Note the different P_z range for the Y-axis in figure 3.8(b) and (c). The comparison of electron momentum distribution is given in figure 3.8(d). For the no electrostatic potential case (black curve in figure 3.8(d)), we find that the full width of the distribution is approximately twice the normalized ponderomotive potential (~ 3.8 MeV). The phase-space trajectory of a single electron in counter propagating EM waves, shown in figure 3.7(a), is consistent with the phase-space density plot of figure 3.8(b). Also, the maximum energy obtained ($\gamma \sim 30$) is consistent in both these simulations. On the other hand, the simulations with a potential well show a larger width of the momentum distribution function (blue and red curve in figure 3.8(d)) indicating higher mean energy. Also, note that increasing the width and depth of potential well results in an increase in electron mean energies. The maximum energy with a potential well is also significantly larger than the case without a potential well. Both these results are consistent with the actual pre-formed plasma scale-length simulation results reported in the previous section. The concentric island-like structures with increasing width along both P_z and Z axes seen in the phase-space density plot (figure 3.8(c)) are due to the increase in energy gain by an electron due to the larger locking distance with either of the waves in the presence of a longitudinal electric field. Again, this trend is clear from the single particle dynamics explained in figures 3.7(c) - (e).

Thus we can explain the plasma heating mechanism for the counter- propagating EM waves in the presence of an electrostatic potential well. The higher mean and maximum energies seen with the longer pre-formed plasma scale-length case can also be explained with this heating mechanism. The larger potential well in the case of long scale-length pre-formed plasma results in the extension of phase-space mixing region, thereby causing an increase in the mean energy with an increase in pre-formed plasma scale-length. The higher maximum energy is essentially due to the longer locking distance with the forward going wave. The longitudinal electric field plays the role of moderator in locking an electron with one of the EM waves by reducing the phase-slippage of the electron with that wave. Finally, we apply this physical picture to the simulations with mobile ions. The

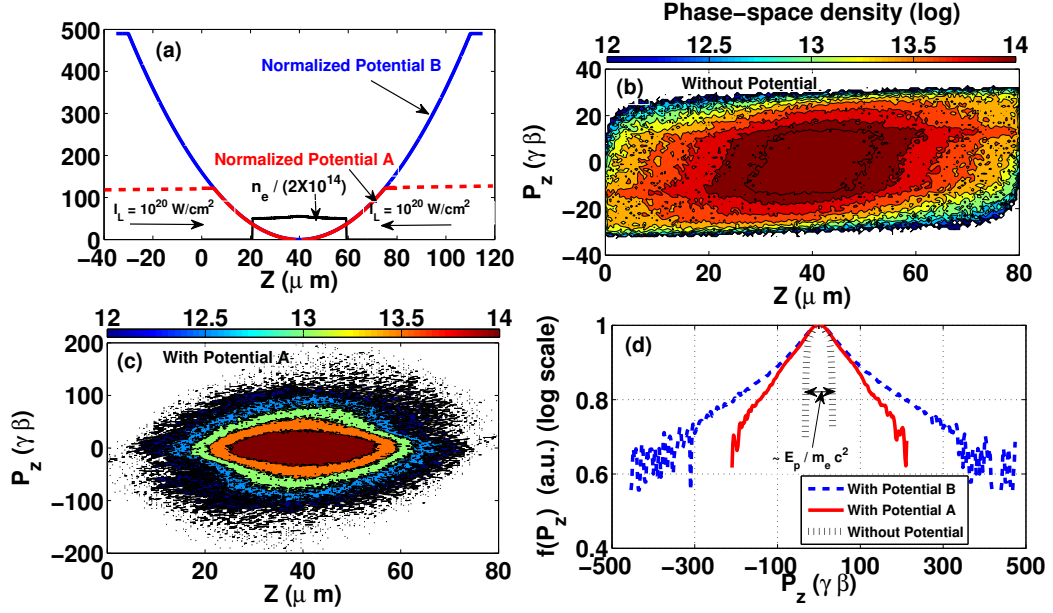


Figure 3.8: Dynamics of plasma heating due to counter propagating EM waves with and without potential well (PIC simulations). (a) Numerical set of the simulation. (b), (c) Phase space density plot for the cases without and with potential well A respectively. (d) Comparison of momentum distribution function for with (blue and red curve) and without (black curve) potential well.

results of mobile ion simulations are discussed in the next section.

3.4 PIC modeling with mobile ions

We now turn our attention to the dynamics in the presence of mobile ions. Fully ionized Aluminum ($Z_i = 13$) is chosen for these simulations. The results of the simulation for an initial $5 \mu m$ pre-plasma density scale-length and laser intensity of 10^{20} W/cm^2 are shown in figure 3.9. In the case of mobile ion simulations, ions are free to respond to the longitudinal electric field on the time scales decided by the charge to mass (Z_i/M) ratio of the ion. The steepening of the plasma density profile near the relativistic critical density surface, similar to recently reported results [Kemp et al., 2009], is observed (figure 3.9(a)). This steepening and the formation of the low-density shelf in front of the relativistic critical density surface can be explained by looking into ion motion (figure 3.9(d)) in the presence of a

longitudinal electric field (figure 3.9(b)) induced due to plasma heating and the resulting electron pressure gradient. The ions near the potential minima ($Z \sim 45 \mu m$) are pushed in both Z -directions, thereby causing a uniform low-density shelf in front of a relativistic critical density surface. Note that the maximum energy of the forward going ions (~ 180 MeV) is consistent with the maximum electrostatic potential ($Ze\phi$). The density of this lower shelf decreases as it expands towards vacuum. This extension of the low-density shelf toward the vacuum results in the widening of the potential well. Extension of the phase-space mixing region of electrons (refer figure 3.9(c)) in the pre-formed plasma due to the wider potential well results in stronger heating of the plasma, which also causes deepening of the potential well (due to increase in plasma electron pressure). The ions are accelerated by the longitudinal electric field caused by the electron pressure gradient. The comparison of mobile ion simulations (figure 3.9(b) and 3.9(c)) with immobile ions simulations (figure 3.6(a)) demonstrates this mechanism. Naturally, we find higher laser absorption in the case of mobile ion simulations compared to immobile ion simulations. For example, for the initial $5 \mu m$ pre-formed plasma density scale-lengths and laser intensity of 10^{20} W/cm², we find approximately 30 % absorption with mobile ions compared to 10 % absorption with immobile ion simulations. Note that laser absorption is determined from laser poynting flux as explained in section-II (refer figure 3.1). The comparison of cumulative electron heat flux going into the target is plotted in figure 3.9(f). The electron heat flux for mobile ion simulations (blue line) is 16 % whereas it is 10 % for immobile ions (red line). The ions carry the rest of the absorbed energy (i.e. 14 % of the total laser energy) in mobile ion simulations. Also, note that almost 80 % of the total electrons heat flux is carried by electrons having energy below 5 MeV for mobile ions due to an increase of the number of fast electrons (refer figure 3.9(e)) in this range.

This trend of increase in the laser absorption with mobile ions continues for other initial pre-formed plasma scale-lengths as well. In figure 3.10 we give laser absorption percentage for various initial pre-formed plasma scale-lengths and laser intensities. In general, we find an increase in the laser absorption with increasing

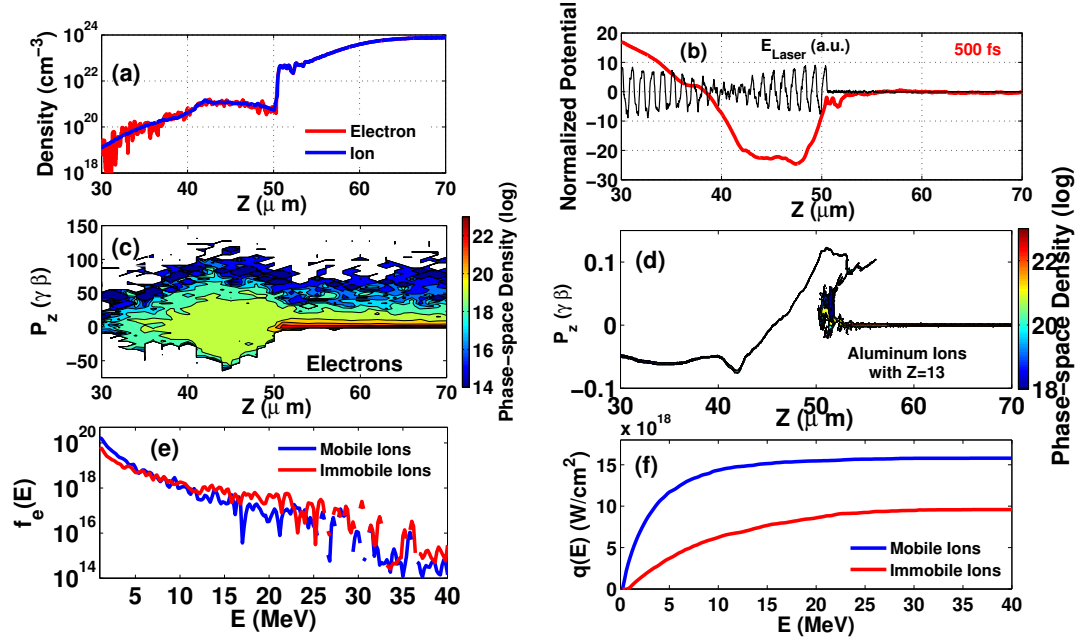


Figure 3.9: Dynamics with mobile ions ($L_p = 5 \mu\text{m}$; $I_L = 10^{20} \text{ W}/\text{cm}^2$). (a) Electron (red line) and ions (blue line) densities. (b) Electrostatic potential well (red line) and laser electric field (black line). (c),(d) The electron and ion phase-space density plots. (e) The inside target electron energy distribution function comparison for mobile (blue line) and immobile ion (red line) simulations. (f) The electron cumulative heat flux comparison for mobile (blue line) and immobile ion (red line) simulations.

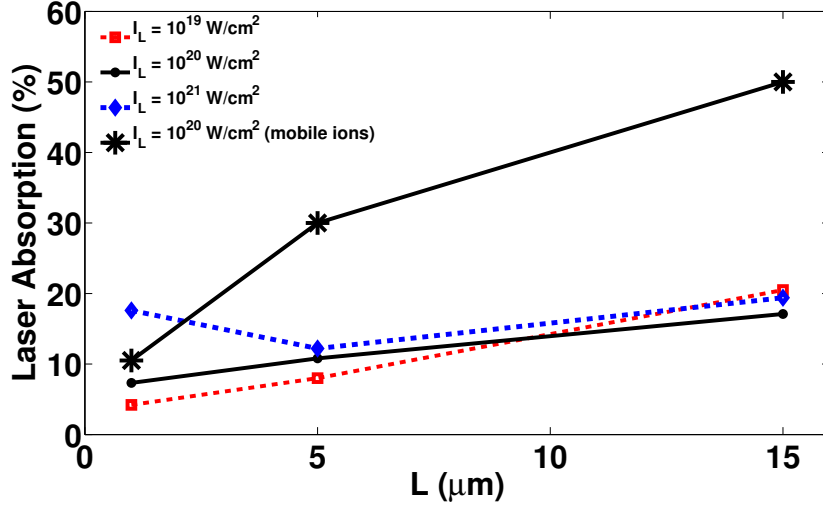


Figure 3.10: Laser absorption for various initial pre-formed plasma scale-length and laser intensities.

pre-formed plasma scale-length as in the case of immobile ion simulations. This is consistent with the physical picture described in this chapter, i.e. larger phase-space mixing region with longer pre-formed plasma due to a wider potential well. Here, we would like to mention that although we see significant increase in laser absorption with mobile ions, the underlying physics of this increase for electrons is the same as that of plasma heating due to counter-propagating EM waves and the presence of an electrostatic potential well described with the help of immobile ion simulations. Also, for the case of laser with 10^{21} W/cm^2 , we observe slightly higher absorption at $1 \mu\text{m}$ scale-length compared to $5 \mu\text{m}$ scale-length. Similar trend is reported in earlier work [Lefebvre and Bonnaud, 1997]. Detailed investigation of this phenomenon will be addressed in future work.

3.5 Conclusions

1-D numerical modeling of laser matter interaction predicts the increase in both the mean and maximum energy of generated fast electrons with the increasing pre-formed plasma scale length for the ranges of laser intensities ($10^{19} - 10^{21} \text{ Wcm}^2$). The stochastic heating of electrons due to counter propagating EM waves

(incident and reflected waves) is found to be the dominant pre-formed plasma heating mechanism. The longitudinal electrostatic potential well, developed self-consistently in the pre-formed plasma, plays a crucial role in the further heating of the electrons. The constant push in one direction by this longitudinal electric field causes reduction in the phase-slip between the electron and one of the EM waves. This finally results in higher energy gains by the locking of the electron with one of the two EM waves. This is found to be the underlying physics behind the higher energy gain in the presence of a longitudinal electric field. The extent of potential well is decided by the pre-formed plasma scale-length. The potential well gets wider with an increase in the pre-formed plasma scale-length, thereby causing extension of the phase-space mixing region. This explains the stronger heating and higher mean energy of generated fast electrons in the presence of a larger pre-formed plasma scale length. The electrons contributing to the high-energy tail of the spectrum come from the under-dense region of pre-formed plasma. These electrons, after getting locked with the forward going EM wave, gain more energy due to longer interaction time (and distance) with the wave. This explains the increase in maximum energy of electrons with the increasing pre-formed plasma scale-length. The effect of ion motion is studied by performing separate simulations with mobile ions. The ions respond to the longitudinal electric potential produced due to plasma electrons heating, which results in the steepening of plasma profile near critical density surface (generally referred to as ponderomotive steepening). The expansion of the low-density shelf towards the vacuum causes the extension of the region of phase-space mixing. Therefore, significant higher absorption is found in the mobile ion simulations compared to immobile ion simulations. The multi-dimensional effects of laser propagation through under-dense plasmas like filamentation, self-focusing, defocusing, etc are neglected in the present 1-D studies. Also, 1-D representation cannot be applied when pre-formed plasma scale-length becomes considerably larger than the laser spot size, which is typically 10-20 μm . Furthermore, it should be noted that results presented in this paper are mainly applicable in the pre-formed plasma scale-length range of 1-15 μm and different laser absorption and fast electrons energy coupling can be expected with extremely

large pre-formed plasma scale-lengths. The strong pre-pulse can damage the solid target. This may constrain the maximum pre-formed plasma scale-length one can expect in the experiments. Finally we would like to point out that, although we see increase in fast electrons energy with increasing pre-formed plasma scale-length, for applications like fast ignition [Tabak et al., 1994] large pre-formed plasma can be detrimental due to shift of relativistic critical surface away from the core. Some of these limitations of present work, especially the multi-dimension effects will be addressed in future studies.

Chapter 3 uses material from the following publication and the dissertation author was the primary investigation and first author of the publication :

B.S.Paradkar, M.S.Wei, T. Yabuuchi, R.B.Stephens, M.G. Haines, S.I. Krasheninnikov and F.N.Beg, “Numerical modeling of fast electrons generation in presence of pre-formed plasma in laser-matter interaction at relativistic intensity”, *Phys. Rev. E* **83** 046401, 2011.

Chapter 4

Mechanism of heating of pre-formed plasma electrons

In the last chapter, we saw that ambipolar electric field present inside pre-formed plasma can play a significant role in the electrons heating. With the help of PIC simulations we demonstrated that the electrons are heated strongly in the presence of longitudinal electrostatic potential well and counter-propagating EM waves. Numerical simulations with the ‘particle pusher’ of a single electron motion in presence of counter-propagating EM waves and potential well demonstrated the stochastic motion of the electron. In this chapter, the detailed study of this stochastic motion and its implication on plasma heating are presented. In particular, we show that such heating can occur even with the presence of a single electromagnetic wave.

This heating resembles the ‘Fermi acceleration mechanism’ [Fermi, 1949] which is generally referred to heating caused by the phase randomization resulting from repeated elastic reflections of particle between fixed and oscillating boundaries [Lichtenberg and Lieberman, 1983]. Similarly, in the case of electron present in the pre-formed plasma, its motion becomes stochastic due to the presence of electromagnetic wave while moving back and forth inside the electrostatic potential well. First we analyze the electron motion inside a ‘V’ shaped infinite potential well (figure 4.1(a)) to demonstrate how a longitudinal electric field influences the stochastic heating of an electron. The constant longitudinal electric field for this

‘V’ type potential well allows us to treat this problem analytically by exploiting the constants of motion. It should be noted that in reality the ambipolar electric field may not be constant inside pre-formed plasma. But as far as the physics of phase randomization during the repeated reflections is concerned, it provides a very simple and concrete framework to study this stochastic heating quantitatively. Finally since in practice the electric field almost vanishes beyond relativistic critical density surface, we extend our results to the finite depth potential well (Figure 4.1(b)) to make quantitative estimates of kinetic energy for electrons leaving out of such potential well and entering the solid as a relativistic electron beam.

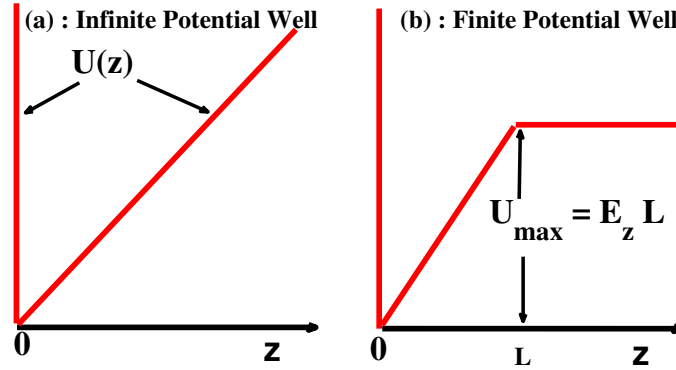


Figure 4.1: Electrostatic potential well chosen for the analysis of electron motion. Fig. (a) represents infinite potential well whereas finite potential well shown in Fig. (b) is used to analyze electron spectrum entering the solid. Perfectly reflecting ‘potential wall’ is assumed at $z = 0$.

4.1 Electron motion inside deep potential well

In this section, we will analyze the motion of the electron inside the deep potential well. By ‘deep’ we mean that the electron can never escape from such potential well. As we reviewed in chapter-2, the relativistic electron dynamics in the presence of a plane laser wave with vector potential $a(t, z)$, propagating along the z -direction and longitudinal electric field E_z , the z -momentum and energy equation

can be written as

$$\frac{d(\gamma V_z)}{dt} = \frac{-1}{2\gamma} \frac{\partial a^2}{\partial z} - E_z \quad (4.1)$$

$$\frac{d\gamma}{dt} = \frac{1}{2\gamma} \frac{\partial a^2}{\partial t} - E_z V_z \quad (4.2)$$

where V_z is the electron velocity component along z direction and the relativistic factor γ is defined as $\gamma = \gamma_A \gamma_z$ with $\gamma_A = \sqrt{1 + a(t, z)^2}$ and $\gamma_z = 1/\sqrt{1 - V_z^2}$. Note that standard normalization is used in the above equations, viz. $t \rightarrow \omega t$, $z \rightarrow kz$, $V_z \rightarrow V_z/c$ and $E_z \rightarrow eE_z/m\omega c$

For a single propagating plane wave of the form $a(t, z) = a(t - z)$, combining Eq. (4.1) and Eq.(4.2) we find

$$\frac{d}{dt}[\gamma_A \gamma_z (1 - V_z)] = E_z (1 - V_z) \quad (4.3)$$

Now, for a constant electric field, the above equation can be integrated to give

$$\gamma_A \gamma_z (1 - V_z) = \delta_0 + E_z (t - t_0 - z) \quad (4.4)$$

where t_0 is the time at which the electron crosses the boundary $z = 0$ and $\delta_0 = \gamma_A \gamma_z (1 - V_z)|_{t=t_0}$. Note that for the highly relativistic case, $\delta_0 \simeq \frac{\gamma_A}{2\gamma_z}$. For simplicity we consider ‘V’-shaped normalized electrostatic potential $U(z)$ (see figure 4.1(a)) which is characterized by a constant electric field, E_z for $z > 0$ and ‘potential wall’ at $z = 0$ where electron is just reflected back preserving its energy. Choice of such a potential well allows us to analyze the electron motion semi-analytically using integrals of motion without loosing essential physics of this heating mechanism.

The trajectory of the electron, $z(t)$ at positive z can be found by introducing a local time $\tau = t - z$ as

$$\frac{dz}{d\tau} = \frac{dz/dt}{d\tau/dt} = \frac{V_z}{1 - V_z} \quad (4.5)$$

Then using V_z from Eq. (4.4) we get

$$\frac{dz}{d\tau} = \frac{f^2(\tau) - 1}{2} \quad (4.6)$$

where $f(\tau) = \gamma_A(t_0 + \tau)/(\delta_0 + E_z\tau)$ Using the above equation, the dynamics of the electron in presence of a ‘V’-shaped electrostatic potential and one plane wave can be studied. The consecutive times t_0 and t_1 at which the electron crosses the boundary $z = 0$ are related by the following equation :

$$\int_0^{t_1-t_0} \frac{[\gamma_A(t_0 + \tau)]^2}{(\delta_0 + E_z\tau)^2} d\tau = t_1 - t_0 \quad (4.7)$$

and the corresponding parameter $\delta_1 = \gamma_A\gamma_z(1 - V_z)|_{t=t_1}$ can be expressed as following

$$\delta_1 = \frac{[\gamma_A(t_1)]^2}{\delta_0 + E_z(t_1 - t_0)} \quad (4.8)$$

Note that, we have used a perfectly reflecting potential wall at $z = 0$, i.e. $V_z(t_1 + 0) = -V_z(t_1 - 0)$. For the case of linearly polarized wave, $a(t, z) = a_0 \cos(t - z)$ and $\delta_0 \ll 1$ (which corresponds to very large energy) the integral in Eq. (4.6) can be solved analytically with the required accuracy of $O(\delta_0) \ll 1$. The detailed derivation is given in Appendix A. Hence, introducing a parameter $\hat{G}_i = [\gamma_A(t_i)]^2/(E_z\delta_i)$ where $i = 0, 1, 2, \dots$, Eq. (4.6) and (4.7) simplify to the following recurrence relations.

$$\hat{G}_i = \hat{G}_{i-1} - \left(\frac{a_0}{E_z}\right)^2 \left\{ \frac{\pi}{2} \cos(2t_{i-1}) + \left[\ln \left(\frac{\hat{G}_{i-1} E_z^2}{2(\gamma_A(t_{i-1}))^2} \right) - C \right] \sin(2t_{i-1}) \right\} \quad (4.9)$$

$$t_i = t_{i-1} + \hat{G}_i \quad (4.10)$$

where C is the Euler constant. Note that in the limit $\delta_0 \ll 1$, \hat{G} is proportional to

the non-dimensional electron kinetic energy, $\varepsilon = \gamma_A \gamma_z \gg 1$. The mapping (4.8,4.9) is rather similar to the ‘Chirikov Standard Map’ [Chirikov, 1979]. Comparing this mapping with the ‘standard map’ we get a_0/E_z as the parameter governing the degree of stochasticity. In particular, the motion becomes stochastic when $a_0 \gtrsim E_z$. This can be seen from Eq. (4.4). The phase slip at which electron stops and gets reflected back can be estimated as $\tau_{stop} \simeq a_0/E_z$. Thus for $a_0/E_z \simeq 1$, the electron bounce frequency inside the potential well becomes comparable with the laser frequency thereby resulting in a transition to stochastic motion. Also, note that the maximum energy step-size can be estimated from Eq. (4.7) as $\sim (a_0^2/E_z) \ln \left(\frac{E_z}{2\delta_0} \right)$. This can be seen by observing that inside the potential well, the change in the electron energy, $\Delta\varepsilon(\tau)$ is given by $\Delta\varepsilon = \gamma_A(\tau)\gamma_z(\tau) + E_z z(\tau) - \gamma_A(0)\gamma_z(0)$ which simplifies into

$$\Delta\varepsilon(t_1 - t_0) = \frac{1}{2} \int_0^{t_1 - t_0} \frac{d(\gamma_A(t_0 + \tau))^2/d\tau}{(\delta_0 + E_z \tau)} d\tau \sim \frac{a_0^2}{E_z} \quad (4.11)$$

Thus the above equation shows that, depending upon the initial phase t_0 of the wave at $z = 0$, the electron will gain or loose energy. Also, for a highly relativistic electron ($\delta_0 \ll 1$), most of the energy is gained when $\tau \ll 1$ i.e. within the first cycle of the wave. The phase shift introduced by the longitudinal electric field is essential for the electron to gain energy in one laser cycle. Thus, the relativistic electrons already traveling at a speed close to the speed of light gains more energy by getting ‘locked’ (i.e. small τ) with the wave.

The analytical predictions discussed above are verified numerically by solving the electron equation of motion for an ensemble of test electrons randomly placed inside the potential well. Figure 4.2 shows the comparison of the Poincare map in (γ, ϕ) space through $z = 0$ obtained numerically with the analytical mapping given by Eq. (4.8) and (4.9). Here the phase ϕ , is defined as $\phi_i = t_i - \pi[t_i/\pi]$, where $[x]$ is the integer part of x .

This agreement shows that mapping Eq. (4.9) and (4.10) correctly describe the electron dynamics for large energies. Mapping given by Eq. (4.9) and (4.10) (refer figure 4.3) demonstrate the transition from regular (Figure 4.3(a), 4.3(b))

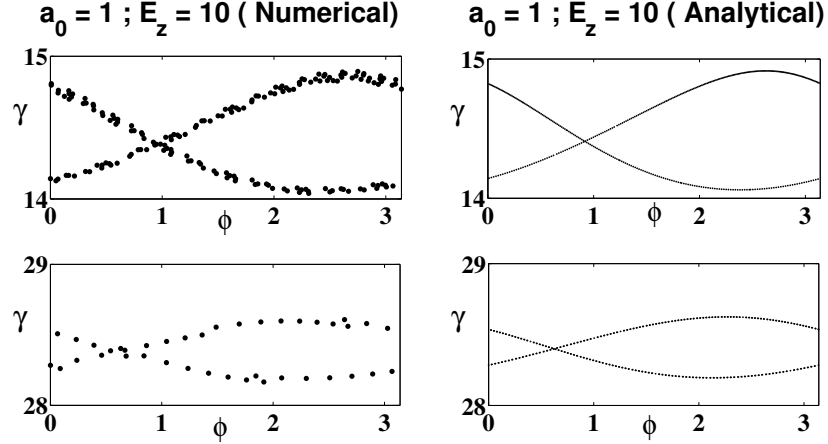


Figure 4.2: Comparison of Poincaré map obtained from numerical calculations and analytical results obtained from Eq. (8) and (9).

to stochastic (Figure 4.3(d)) motion, with increasing a_0/E_z ratio. The effective threshold of this transition, given by $a_0/E_z \sim 1$, can also be seen in figure 4.3. Physically this means that when $a_0 \gtrsim E_z$, the electron sees a random initial phase of the electromagnetic wave for each successive arrivals at $z = 0$. On the hand, for the case of $a_0/E_z < 1$, the phase varies adiabatically for successive reflections resulting in regular motion.

For the highly stochastic regime i.e. $a_0 \gg E_z$, electron heating can be described by diffusion [Chirikov, 1979] in energy space ε , ($\gamma \gg 1$). For this case, the elementary step-size in energy space $\delta\gamma$, and time δt , can be estimated as $\delta\gamma \sim (a_0^2 \Lambda)/E_z$ and $\delta t \sim \gamma/E_z$ where $\Lambda \sim \text{constant}$, is a slowly varying logarithmic function on the right hand side of Eq. (4.9). As a result, the energy diffusion coefficient can be estimated as $D_\gamma \sim (\delta\gamma)^2/\delta t \sim (a_0^2 \Lambda)^2/(\gamma E_z)$. With such a diffusion coefficient, the asymptotic time evolution of the averaged electron energy $\langle \varepsilon \rangle$, and the electron distribution function, $f(\varepsilon, t)$, is given by the following expressions :

$$\langle \varepsilon \rangle \sim \langle \gamma \rangle \sim (D_\gamma t)^{1/3} \quad (4.12)$$

$$f(\varepsilon, t) \sim t^{-1/3} \exp\left(\frac{-\varepsilon^3}{9D_\gamma t}\right) \quad (4.13)$$

The analytic estimates for this regime which correspond to the case of a large scale-

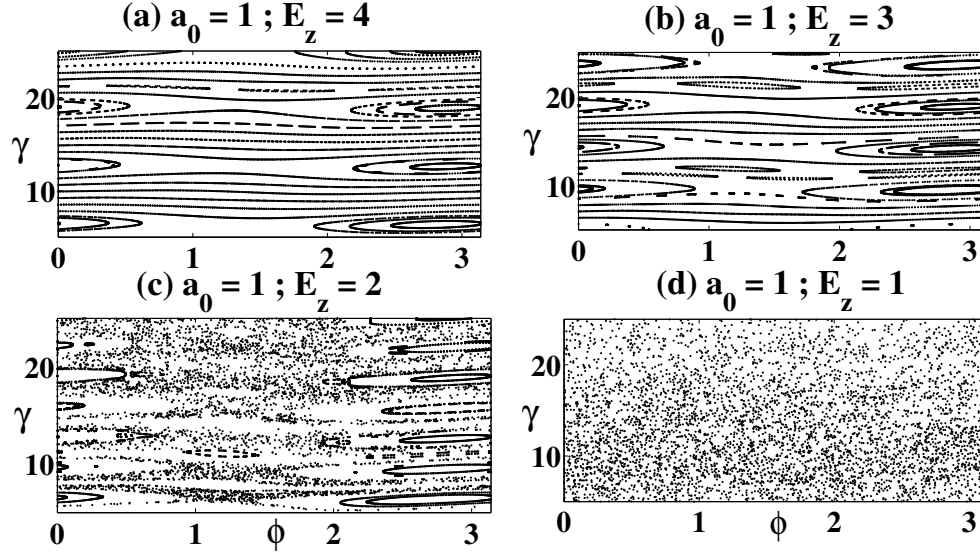


Figure 4.3: Poincaré map in (γ, ϕ) space for different values of a_0/E_z . Transition from strictly periodic motion (Fig. (a) and (b)) to stochastic motion (Fig. (d)) with increasing values of a_0/E_z is clearly demonstrated here.

length pre-formed plasma are verified numerically. The temporal dependance of the average energy of the test electrons, placed inside an infinite potential well, is plotted in figure 4.4 which is in agreement with Eq. (4.12).

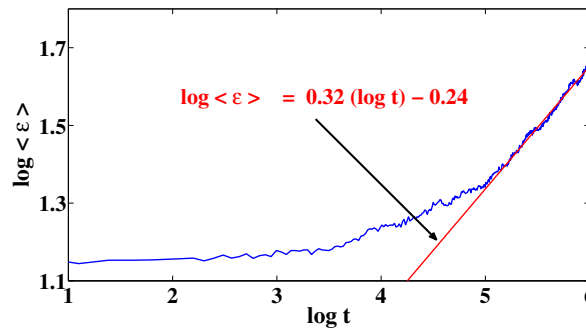


Figure 4.4: Average energy of electrons inside potential well vs time (numerical calculations) confirming $t^{1/3}$ dependance predicted by Eq.(4.12).

4.2 Electron heating in finite depth potential well

To address the issue of the energy of electrons generated in the pre-formed plasma and entering the solid target, we need to consider the potential well of finite depth (see fig. 4.1(b)) and analyze the energy distribution of electrons coming out of the well. We will assume that the ‘depth’ of the potential well, $U_{max} = E_z L$ is larger than the energy space diffusion step-size, i.e. $U_{max} > \delta\gamma \sim a_0^2/E_z$ and electron motion in the well is stochastic i.e. $a_0 > E_z$. The electron inside such a potential well will get heated up while performing a ‘random walk’ in energy space until it is thrown out of the well. The energy gained by the electron during the last transit from $z = 0$ can be estimated from Eq.(4.11). Thus, the total energy of the electron beam leaving the potential well can be estimated as $\gamma = 1 + \alpha(a_0^2/E_z)\Lambda$, where $\alpha \sim 1$ is the numerical factor and Λ is the logarithmic function described before.

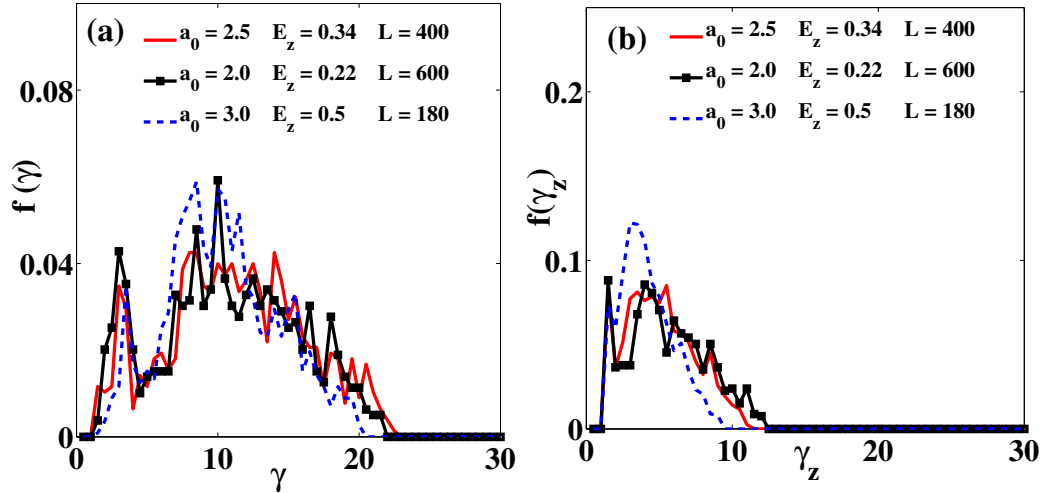


Figure 4.5: Energy distribution functions for total energy (Fig. (a)) and parallel energy (Fig. (b)) of electrons escaping the finite depth potential well for different a_0 values such that elementary energy-step size, a_0^2/E_z is constant.

In our model, the escaping electron has both perpendicular ($\gamma_A \sim a_0$) and parallel ($\gamma_z \sim a_0/E_z$) energy components. In reality, beyond relativistic critical density ($z = L$), the laser field quickly goes to zero which in 1-D case results

in conversion of perpendicular energy into parallel energy. This process causes additional ponderomotive acceleration with the energy gain $\simeq \beta a_0$. β is a numerical factor ~ 1 . Thus the electron beam enters the solid with only the parallel energy given by $\gamma_{beam} = 1 + \alpha(a_0^2/E_z)\Lambda + \beta a_0$ which in highly stochastic regime can be much greater than the laser ponderomotive energy $\gamma_{ponder} = \sqrt{1 + a_0^2}$ in agreement with experimental and numerical results. Note that beam energy can not exceed U_{max} . Numerical calculations for a finite potential well confirm these predictions. The distribution of the electrons at the end of the potential well for different values of a_0, E_z and L , but keeping $\delta\gamma \sim a_0^2/E_z$ constant show that the maximum γ and γ_z at $z = L$ scales proportional to a_0^2/E_z and a_0/E_z respectively (see figure 4.5).

4.3 Conclusions

In summary, we analyze the heating mechanism of pre-formed plasma electrons due to the relativistic laser radiation and longitudinal electric field with a ‘V’ shaped potential well. Based on our theoretical results and numerical simulations, we conclude that: i) For $a_0/E_z \gtrsim 1$, the electron motion in the laser and longitudinal electrostatic field becomes stochastic for deep potential well. ii) In the highly stochastic regime ($a_0/E_z \gtrsim 1$), the electron undergoes energy space diffusion with the characteristic step-size $\sim a_0^2/E_z$ and the energy of the electron beam entering the solid is estimated as $\gamma_{beam} = 1 + \alpha(a_0^2/E_z)\Lambda + \beta a_0$ which is much larger than the ponderomotive energy.

Chapter 4 uses material from the following publication and the dissertation author was the primary investigation and first author of the publication :

B. S. Paradkar, S. I. Krasheninnikov and F. N. Beg, “Mechanism of pre-formed plasma electrons heating in relativistic laser-solid interaction”, submitted to *Phys. Rev. Lett.*.

Chapter 5

Fast electron transport studies in presence of long scale length pre-formed plasma

In last two chapters we discussed the fast electrons generation in presence of pre-formed plasma. Now, we look into the problem of influence of this pre-formed plasma on the transport of this energetic relativistic electrons into the solid target. In particular, the results of numerical modeling of the experiment [Yabuuchi et al., 2010] carried out to investigate the effect of long scale pre-plasma on fast electron transport are presented. A peculiar ring-like structure in Cu $K\alpha$ x-ray emission was seen in this experiment when a short pulse laser (intensity $\sim 3 \times 10^{18}$ W/cm²) interacted with a long scale pre-plasma. The long scale pre-plasma was produced by irradiation of a long pulse laser on a flat target having copper fluorescence layer sandwiched between aluminum layers. The details of radiation hydrodynamic simulations (for the production of pre-formed plasma), hybrid-PIC modeling (for the fast electrons transport) along with the physics of this experimentally seen ring structure is discussed in this chapter.

5.1 Introduction

Understanding the transport of fast electron is extremely important for the successful realization of electron fast ignition scheme of inertial confinement fusion. The efficiency with which the fast electrons deposit their energy into the compressed core depends upon the transport of these electrons from the pre-formed plasma into the high density core. Since the critical density surface moves away from compressed core due to expansion of pre-plasma into vacuum, fast electrons have to travel a longer distance before they deposit their energy in the core. Also, due to divergence of the generated fast electrons beam, increase transport distance will result in reduction of effective intensity of the beam when it reaches the core region. These effects can be detrimental for the success of fast ignition. Especially for the full scale cone guide fast ignition, we should expect long scale-length pre-formed plasma inside the cone due to geometric effects based on present day experiments[Baton et al., 2008, MacPhee et al., 2010, Van Woerkom et al., 2008]. But in these experiments the presence of the cone precludes direct observation of the pre-plasma created by the pre-pulse. This problem can be eliminated by performing the experiments with flat foils instead of cone shaped targets and creating a long scale-length pre-formed plasma with the separate long pulse laser which irradiates the target before the arrival of short pulse laser. The fast electrons transport can then be diagnosed by measuring the $K\alpha$ x-ray emission from the copper fluorescence layer sandwiched between two solid targets. This line x-ray emission (from $n = 2$ to $n = 1$) is due to the vacancies created in the inner shells of copper atoms by the energetic fast electrons.

Taking these things into considerations, an experiment [Yabuuchi et al., 2010] (see figure 5.1(a)) was carried out at the GMII laser facility at Osaka University. Long scale length pre-plasma was created by focusing a separate long pulse laser ($1 \mu m$ wavelength, 0.5 J, $200 \mu m$ dia. spot, 0.5ns (FWHM)) on a multilayered flat target (transverse dimension: 1mm) comprised of aluminum ($10 \mu m$)/copper ($25 \mu m$)/ aluminum (1 mm). The pre-formed plasma density profile was measured with an optical (laser) interferometer. Fast electrons produced from the short pulse laser ($1 \mu m$ wavelength, 12 J, $20 \mu m$ FWHM spot, 600 fs FWHM

duration, peak laser intensity $\sim 3 \times 10^{18}$ W/cm²) interaction with the target were investigated by measuring Cu K α x-rays emission from the Cu fluorescence layer with a 2D spatial imager from the target front side. The angles of incidence of short and long pulse laser with respect to the target normal are 25° and 30° respectively. One interesting feature observed in the 2D Cu K α imaging was the annular ring-like Cu K α x-ray emission pattern (as shown in figure 5.1(b)) which was observed only when the target was irradiated with the short pulse laser in the presence of the large pre-plasma formed by the long pulse laser. A radial lineout (figure 5.1(d)) shows that the ratio of peak intensity of central spot to the intensity of outer annular ring is approximately 15:1. This ring structure was not seen in a short pulse only interaction, which lacks a large pre-plasma (figure 5.1(c)). Also, it should be noted from figure 5.1(d) that the outer ring has the diameter of about 450-500 μ m whereas the central K α spot has the diameter of around 50 μ m (of the same order of short pulse laser spot size).

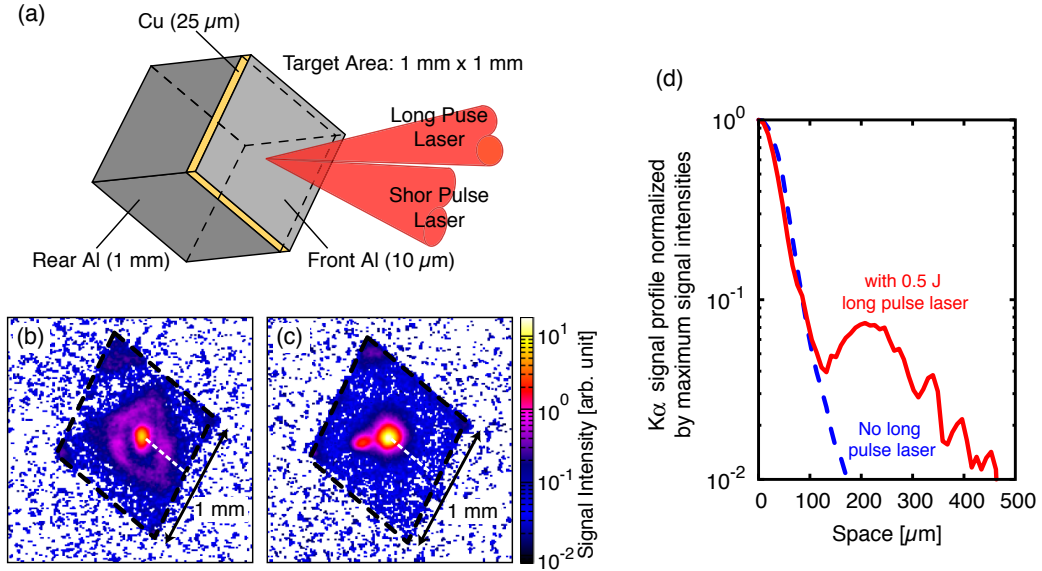


Figure 5.1: (a) A schematic of the target with both long and short pulse laser beams. (b) Annular ring-like structure was seen in Cu K α x-ray emission in the presence of pre-plasma. (c) No outer ring was observed without pre-plasma. (d) Lineouts of the fluorescence image for shots with and without pre-plasma are shown by solid red and dotted blue lines respectively. These lineouts are taken along the white dashed lines drawn in (b) and (c).

In case of short pulse ultrahigh intensity ($\sim 10^{19}$ W/cm²) laser matter interaction, an annular ring was observed in the experiments [Koch et al., 2001]. According to theoretical model [Davies et al., 2006] suggested for this experiment, the self consistently generated magnetic fields that push the electrons towards higher resistivity regions lead to hollowing of the beam. However, laser intensities used in these simulations were much higher ($\sim 5 \times 10^{19}$ W/cm²) than in the experiment mentioned above; high fast electron current density is required to create a low resistivity region by Ohmic heating in the central region. But, as mentioned earlier, in our experiment no ring structure was seen when only the short pulse laser was irradiated on the solid target. Therefore, the mechanism proposed by Davies et al is not relevant to explain our experimental observation.

Ring-like structures in x-ray emission were also observed with an x-ray pinhole camera in some of the early long pulse laser matter interaction experiments where the laser intensity was on the order of $10^{15} - 10^{16}$ W/cm² [Amiranoff et al., 1982, Burgess et al., 1985, Jaanimagi et al., 1981, Kieffer et al., 1983, Luther-Davies et al., 1987]. Numerical simulations by Forslund and Brackbill [Forslund and Brackbill, 1982], followed by several other publications [Fabbro and Mora, 1982, Wallace, 1985, Wallace et al., 1986] attributed this experimental observation to lateral spreading of thermoelectric azimuthal magnetic field [Max et al., 1978]. According to these simulations, the observed rings are produced during the coronal plasma expansion into vacuum. During this phase, the supra-thermal electrons ($\sim 10 - 20$ keV), generated mainly due to the resonance absorption, undergo lateral transport in coronal plasma due to the $E \times B$ drift. The electric field (E) in this case, is generated during the self-similar expansion of coronal plasma into vacuum [Crow et al., 1975, Mora and Pellat, 1979] and therefore is directed normal to the plasma boundary. The azimuthal magnetic field is produced by usual $\nabla T \times \nabla n$ mechanism [Max et al., 1978]. Thus, presence of this radially expanding magnetic field effectively shields these supra-thermal electrons from interacting with high density solid. Therefore, the electrons initially travelling laterally during the phase of expansion of coronal plasma are eventually pulled back to the solid target at a radial distance away from the laser spot where shielding is ineffective

due to the reduced magnetic field. Hence, this mechanism could explain not only the formation of a ring but also the experimental observation of an increase in ring radius along with the expansion of coronal plasma in vacuum. Also, these simulations suggested that the fast electrons would return back to the target at the pre-plasma edge. But since the pre-plasma density was assumed to be uniform in the transverse direction, the fast electrons were always reflected at the distinct plasma-vacuum boundary introduced in these numerical simulations.

Here, we have modeled the ring-like x-ray emission seen in our experiment with realistic a pre-plasma having both longitudinal and transverse density gradients. Therefore, this work revisits the earlier mechanism for the lateral transport of fast electrons with more accurately modeled pre-formed plasma density profile. A detailed investigation of mechanism of fast electron reflection near the transverse plasma-vacuum boundary is presented in this chapter. A radiation hydrodynamic code is used to simulate pre-plasma creation including the thermoelectric B-field, and a hybrid PIC code is used to investigate fast electron transport in the solid target with the presence of the pre-formed plasma.

5.2 Hydrodynamic modeling of the pre-plasma creation

We have simulated pre-formed plasma creation with a 2-D three fluid Lagrangian radiation hydrodynamic code, h2d¹. The code solves the basic fluid conservation equations of mass, momentum and energy [Braginskii, 1965] with MHD approximation in Lagrange coordinates. The three fluids are designated as the free electrons, the material species (fully/partially ionized or neutral) and the radiation field. The electron and ions species are coupled to each other via Coulomb collisions. Mass conservation is guaranteed since h2d is a Lagrangian code. The electron and ions fluid momentum conservation equation contains $J \times B$ term due to magnetic fields apart from the usual stress tensor term of Navier-Stokes

¹h2d is a commercial product of Cascade Applied Sciences Incorporated, 6325, Trevarton Drive, Longmont, CO,80503, USA (e-mail: Larsen@casinc.com).

equation. A magnetic induction equation [Braginskii, 1965] is used to advance magnetic field in time. The electron and ions thermal energy transport is modeled with Spitzer/Braginskii transport coefficients. The code uses the various models for Equations Of State (EOS) such as ideal gas model, Thomas-Fermi model, SESAME EOS tables, etc. Finally radiation transport is treated with either single group (Gray diffusion) approximation or multi-group approximation. The radiation field is essentially coupled to electron fluid. Simulations are run in axi-symmetric R-Z cylindrical geometry with the Z-axis aligned in the direction of laser propagation. The 0.5 ns (FWHM) long pulse laser (wavelength $1\ \mu\text{m}$) with energy of 0.5 J and spot diameter of $200\ \mu\text{m}$ (FWHM) is incident on a flat solid target comprising of front aluminum ablator and back copper layer. Here, we would like to point out that although in the actual experiment the long pulse laser was incident on the target with a 25 angle relative to the target normal direction, in these simulations we have modeled the normally incident laser due to the cylindrical symmetry employed in the code. The 1 mm thick aluminum back layer is not included since the long pulse laser energy is too low for its shock front to reach this layer prior to the arrival of the short pulse beam (this thick Al layer is included in the hybrid PIC modeling described in the next section to prevent refluxing of the fast electrons). h2d simulation results confirm this assumption. The intensity of the long pulse beam is about $10^{13}\ \text{W}/\text{cm}^2$. SESAME EOS ² tables are used for both aluminum and copper. Multi-group radiation transport model is used with 30 photon groups, arranged logarithmically between energies of 5 eV to 10 keV. Thomas-Fermi ionization model and electron conduction flux limiter of 0.06 [Goncharov et al., 2006] is used in the simulations. Also, azimuthal thermoelectric magnetic fields generated by mechanism are computed self-consistently. Figure 5.2 shows the contour plots of the simulated plasma electron number density, temperature and azimuthal magnetic fields generated at the time of short pulse injection (260 fs after the peak of the long pulse laser). The hydro simulations suggest that the on-axis pre-formed plasma density (n_e) scale length, defined as $L \sim n_e/\nabla n_e$, near the critical surface

²See National Technical Information Service Document No DE94011699 SESAME database by Johnson J D Los Alamos National Laboratory Report No LA-UR-94-1451, 1994. Copies may be ordered from National Technical Information Service, Springfield, VA 22161, USA

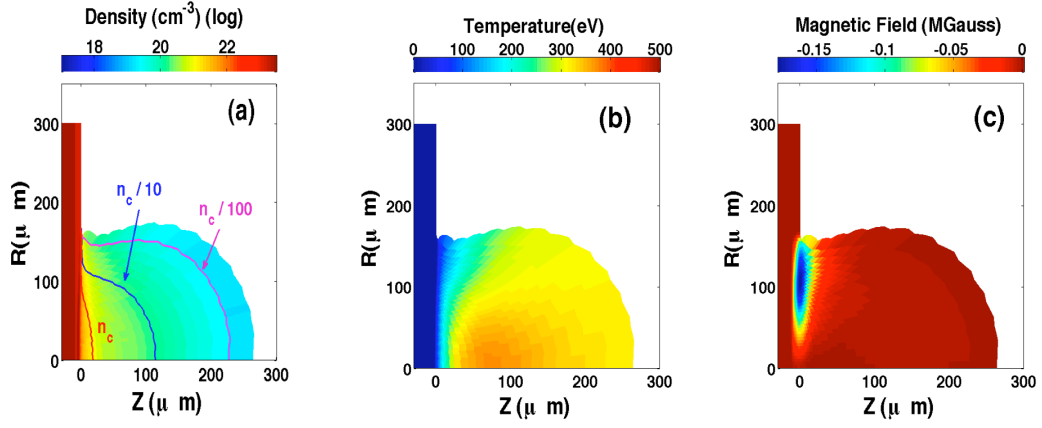


Figure 5.2: Simulated pre-formed plasma with the radiation hydrodynamic code, h2d at the time of injection of short pulse laser. Initial target front surface is at $z = 0 \mu m$. (a) Plasma electron density profile (b) Plasma electron temperature profile and (c) Azimuthal thermoelectric magnetic field. A negative value of magnetic field implies that the field is going into the plane of the paper (clockwise direction around the z -axis).

is about $9 \mu m$ when the short pulse laser beam is injected. The critical density surface is $17 \mu m$ in front of the target surface. The two dimensional (2-D) nature of coronal plasma expansion is evident from figure 5.2(a) which shows the gradient of density is much higher in the transverse direction (beyond laser spot size) than the longitudinal direction.

The axial, as well as radial lineouts of the simulated plasma density, match well with the experimentally measured density determined by laser interferometry [Yabuuchi et al., 2010] in the range of $5 \times 10^{19} - 5 \times 10^{18} \text{ cm}^{-3}$. The average ionization level in the front aluminum layer calculated from h2d simulations is 2-3 whereas most of the coronal plasma is fully ionized. The coronal plasma predominantly expands isothermally with electron temperature in the range of 300-500 eV. The 2-D nature of its expansion can be seen from the fall in temperature beyond laser spot radius (i.e. $100 \mu m$) in the coronal plasma. The simulated peak azimuthal magnetic field of 0.21 MG is consistent with steady state estimates for thermoelectric magnetic fields [Max et al., 1974]. The steady state magnetic field is established by the balance of the $\nabla T \times \nabla n$ source term and convection of this magnetic field due to coronal plasma flow. Thus, steady state magnetic field scales

as

$$\left(\frac{B}{10^6 Gauss}\right) \approx 30 \left(\frac{T_e}{1 keV}\right)^{1/2} \left(\frac{1 \mu m}{L_T}\right) \left(\frac{A}{Z}\right) \quad (5.1)$$

For fully ionized aluminum with $T_e = 300$ eV, temperature scale length $L_T = 200 \mu m$ (long pulse laser spot size), the steady state magnetic field would be around 0.17 MG; this agrees well with the simulated peak magnetic field value of 0.21 MG (figure 3(c)). Also, it can be seen from simulations that the ablation front is still inside the front aluminum layer, which means that the copper layer is protected from direct short pulse laser illumination. The calculated plasma conditions (density, temperature and magnetic field) are then included in the hybrid PIC simulation as its initial condition.

5.3 Fast electron transport modeling with hybrid PIC code, LSP

5.3.1 LSP simulation set up

The hybrid PIC code, LSP [Welch et al., 2001, 2006] is used to model the fast electron transport. The simulations are run in 2-D axi-symmetric R-Z cylindrical geometry with the Z-axis aligned with the direction of laser propagation. Due to the approximate symmetry of coronal plasma expansion about the laser propagation axis, the cylindrical geometry used in our simulation provides a reasonably realistic 2-D representation of the actual 3-D problem. The 2-D Cartesian geometry on the other hand, assumes either no variation in the third dimension or infinite third dimension; neither of which is a valid assumption when the long pulse laser spot size (200 μm FWHM) is comparable with the transverse target dimension (1 mm). LSP employs an implicit differencing scheme, which unlike conventional explicit algorithms allows a grid resolution (Δ_x) greater than Debye length (λ_D) without causing excess numerical heating. Hence, this approach is ideally suitable for simulating high-density plasmas. The hybrid algorithm allows

energy and momentum conserving fluid description of background plasma along with kinetic treatment of the fast electrons. Thus, good overall energy and momentum conservation can be obtained without the need to resolve the plasma Debye length. Accordingly, the time step constraint turns out to be $c\Delta_t < \Delta_x$ where c is velocity of light. For the present simulations we have employed uniform grid resolution of $0.5 \mu m$ in both R and Z direction and time step of $c\Delta_t \sim 0.05 \mu m$. The numerical results are verified by running a high-resolution simulation ($0.1 \mu m$ in both directions) for a relatively smaller duration (~ 1 ps). Performing laser-plasma interaction simulations is extremely difficult even for modern day super-computers due to the large extent of pre-plasma ($\sim 200 \mu m$ in both radial and axial directions) formed during long pulse interaction. Such long scale problems can be effectively handled with hybrid PIC simulation approach [Evans, 2007]. Since we are mainly interested in fast electron transport in the presence of pre-formed plasma, transport can be studied by injecting fast electrons at the relativistic critical density surface. Possible changes in the electron source divergence caused by laser interaction with the plasma-self-focusing, filamentation, etc. have been addressed by performing a series of simulations with different fast electron divergence angles (ranging from 10° to 60° half angles) as described later. The typical spectrum of these injected electrons can be obtained from various scaling laws such as the ponderomotive scaling [Wilks et al., 1992] and Begs empirical scaling [Beg et al., 1997]. The intensity profile in the short pulse laser beam focal spot is modeled, as usual, with a double Gaussian-like spatial distribution, i.e., high intensity in a small spot (a few times the diffraction limit) containing most of the laser energy and a low intensity large spot to count for the energy in the wing region. The laser beam is modeled by superposition of two Gaussian beams, each carrying 50 % of the total laser energy. For the high intensity central spot a narrow Gaussian beam ($20 \mu m$ FWHM, 2.5×10^{18} W/cm² peak intensity) extending up to $20 \mu m$ is used; the low intensity outer wing is modeled by another Gaussian beam ($50 \mu m$ FWHM, 3×10^{17} W/cm² peak intensity) extending up to $50 \mu m$. The superposition of these two Gaussian profiles effectively gives on axis ($R = 0 \mu m$) peak laser intensity of 2.8×10^{18} W/cm² with central spot of $20 \mu m$ containing

65 % laser energy and the rest of the 35 % of energy in the outer halo (from $R = 20 \mu m$ to $R = 50 \mu m$). Therefore, the energy contributions by broad Gaussian to the central region and narrow Gaussian to the wing region are insignificant. The laser to fast electron energy conversion efficiency and mean electron energy (T_{hot}) are calculated based on peak intensity of individual Gaussian beams. Two fast electron beams are injected corresponding to each of these Gaussian profiles. The laser energy to fast electron energy conversion efficiency (η) is taken as 13 % for central narrow Gaussian and 7 % for broad Gaussian, computed from the experimentally determined scaling[Town et al., 2005]

$$\eta = 0.000175 \times I_{Laser}^{0.2661} \quad (5.2)$$

Hence for short pulse laser energy of 12 J, the energy contained in narrow and broad Gaussian electron beams is 0.78 J and 0.42 J respectively. This gives an overall conversion efficiency of 10% and the electron energy in the central $20 \mu m$ spot comes out to be 0.9 J. In the next step, the mean energy of fast electrons (T_{hot}) is calculated from Beg scaling[Beg et al., 1997] using the formula

$$T_{hot}(keV) = 100 \left(\frac{I(W/cm^2)\lambda(\mu m)^2}{10^{17}} \right)^{1/3} \quad (5.3)$$

Here, it should be noted that in our calculations both the estimates of conversion efficiency and average fast electron temperature are based on the peak intensity of two Gaussian beams. The mean energy of fast electrons in narrow and broad Gaussians is about 300 keV and 170 keV respectively. Also, it should be noted that some of the generated electrons in the presence of long scale-length pre-formed plasma can have energies significantly greater than that given by ponderomotive scaling or Beg scaling. These electrons are not included in the present injection model. Finally, the total fast electron beam current density can be calculated by dividing the total fast electron energy flux by the mean fast electron energy using the formula,

$$J_{hot} = \eta(I_{Laser})/T_{hot} \quad (5.4)$$

The corresponding peak fast electron current densities are 1.13×10^{12} A/cm² and 1.23×10^{11} A/cm² respectively. In modeling this situation, the fast electron energy distribution is assumed to be of form $\exp -E/T_{hot}$. The electrons are randomly injected within a divergence half-angle of $\theta_{1/2}$. The results shown in section 5.3.2 are for the case with the fast electron beam divergence $\theta_{1/2} = 30^\circ$ [Stephens et al., 2004]. Thus, two electron beams with 0.5 ps FWHM Gaussian temporal variation are injected at 3 times the relativistic critical surface for better numerical stability. The relativistic critical density is calculated using the formula

$$n_{cr}(cm^{-3}) = \gamma_{osc} \left(\frac{1.1 \times 10^{21}}{\lambda_{\mu m}} \right) \quad (5.5)$$

where the relativistic Lorentz factor, γ_{osc} is defined as $\gamma_{osc} = \sqrt{1 + a_0^2/2}$, a_0 being the normalized vector potential of the laser field. The plane of electron beam injection is located at $Z = 5 \mu m$ where background plasma density is around 4×10^{21} cm⁻³. The background plasma density variation in the plane of injection i.e. from $(R, Z) \equiv (0, 5) \mu m$ to $(R, Z) \equiv (50, 5) \mu m$ is negligible due to large spot size (FWHM = 100 μm) of long pulse laser (refer figure 5.2). The LSP calculations with injection model were found to be numerically stable when peak density of fast electrons ($\sim 3 \times 10^{20}$ cm⁻³) was at least ten times less than the background plasma density. Since the relativistic critical density surface is located on axis at $Z = 8 \mu m$, the plane of injection ($Z = 5 \mu m$) is moved by 3 μm from the actual fast electron source. Hence, injecting fast electron beam at 3 times the relativistic critical density surface allowed us to perform stable calculations without compromising much on the exact location of the relativistic critical density surface.

Figure 5.3 shows the initial set up and background plasma condition used in the LSP simulations. A Perfectly Matched Layer (PML) free-space boundary condition is employed to take out all the particles and fields extending to the edge of the simulation box. Due to the long pre-plasma density scale length in the axial (Z) direction, one can expect no significant electrostatic field excitation by fast electrons travelling in this direction into the low-density plasma. This assumption was validated by running 1-D LSP simulations using a fully extended

background plasma ($\sim 600 \mu m$) having density gradient scale-lengths equal to axial density scale-length predicted by hydro-simulations. Therefore the PML free-space boundary condition can be applied at the right side of simulation box (.e. at $Z = 120 \mu m$ as shown in figure 5.3). Since mass inside the mesh is conserved in a Lagrangian code, the size of the mesh increases as it expands into vacuum to form the low-density plasma. This results in poor numerical spatial resolution of very low-density coronal plasma, simulated by hydro-code. Therefore, while inputting densities obtained from hydro-code into LSP calculations we have extended the pre-plasma down to densities on the order of 10^{14} cm^{-3} in the transverse (R) direction with an exponential fall of the form $n(Z, R) = n_{edge} \exp -R/L_T$ where n_{edge} is the well resolved density of pre-plasma at the plasma transverse edge obtained from hydro-simulations and L_T is the scale length of the extended plasma density gradient. L_T is taken to be equal to the scale length of pre-plasma density gradient in the transverse direction at the plasma edge, i.e. $\frac{1}{L_T} = \left(\frac{1}{n_{edge}} \right) \left(\frac{\partial n}{\partial R} \right) |_{R_{edge}, Z}$. As mentioned in the previous section, the aluminum layer behind the copper layer is included in these simulations.

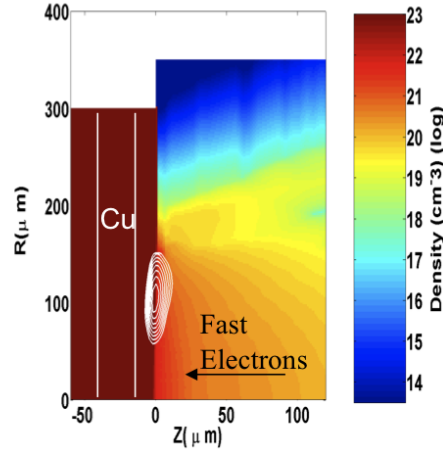


Figure 5.3: Initial background plasma condition used in the LSP simulation. Fast electrons are injected at $3 \times$ relativistic critical density surface. Thermoelectric azimuthal magnetic fields (shown in figure 5.2(c)) are represented by white contour lines.

5.3.2 Hybrid PIC simulation results and discussion

The early stage of electron beam injection is shown in figure 5.4. In this figure we have zoomed in on the beam injection region in order to clearly identify the fields. A strong axial electric field is excited due to charge separation at the relativistic critical density surface (figure 5.4 (b) and (e) at time 0.1ps and 0.3 ps respectively). Positive ions left behind at the relativistic critical surface are responsible for this charge separation. Therefore, this longitudinal electric field (E_z) is directed away from the plane of injection (shown by dotted lines in figure 5.4(b)). Similar longitudinal electric fields are discussed in recent laser-plasma interaction simulations [Kemp et al., 2009, Sherlock, 2009]. In addition, azimuthal magnetic field (of positive polarity) seen in figure 5.4(c) in between $Z \sim 4 \mu m$ and $Z \sim 6 \mu m$ is produced by uncompensated fast electron beam current ($\nabla \times \vec{B} = (4\pi/c) \vec{J}_{beam}$) in this region. These magnetic fields (~ 5 -20 MG) are large compared to the thermoelectric magnetic field (~ 0.2 MG) produced in long pulse interaction. This crossed electric and magnetic field results in a radial spread of fast electrons as can be clearly seen from figure 5.4(d). Note that the negative polarity magnetic fields on either side of the positive magnetic field in figure 5.4(c) are consistent with corresponding radial currents produced by $E \times B$ drifts. Due to the finite extent of this region ($\sim 2 \mu m$), only the low energy electrons undergo this radial drift resulting in the transport parallel to target surface. The electrons having higher parallel energy enter the target without any significant deflection in radial direction. For example, 80 keV electrons will have relativistic Larmour radius of $1 \mu m$ for a typical azimuthal magnetic field 10 MG. Since the spatial extent of these magnetic fields is approximately $2 \mu m$, one can expect that electrons with energy greater than 80 keV will pass through this region without any significant deflection. Also, although the electron beam is injected into the plasma in the direction of the laser propagation, some of the lower energy electrons are reflected back into coronal plasma due to strong electric and magnetic fields in the injection region. Similar bottlenecking of fast electrons is seen in earlier laser plasma interaction simulations [Wei et al., 2008]. The alternating polarity of the azimuthal magnetic field seen in figure 5.4(f) suggests the electrons would filament in the radial direction due

to electromagnetic Weibel instability [Yoon, 1989] in a counter-propagating beam-plasma system.

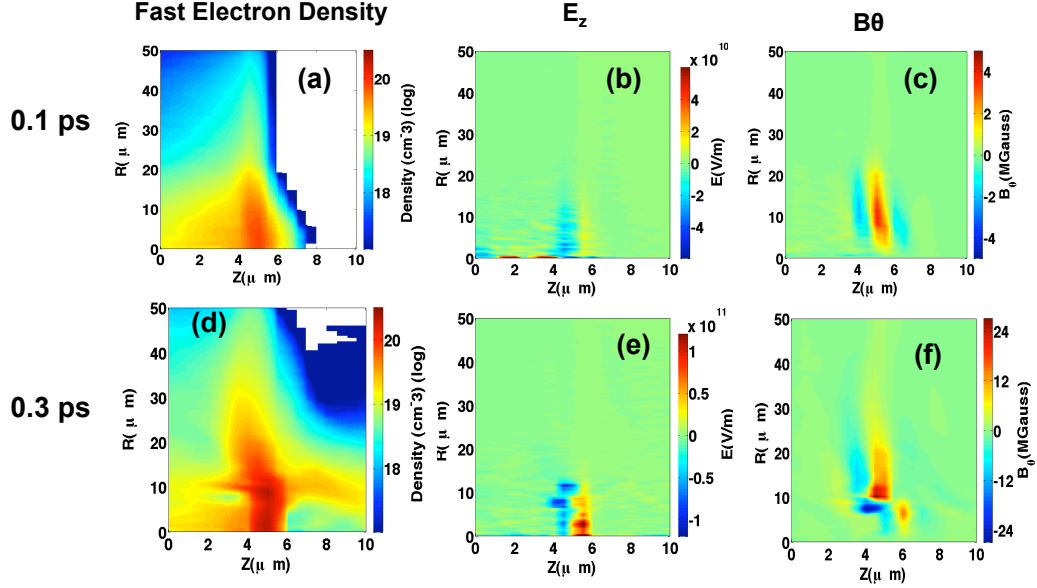


Figure 5.4: Early stages of fast electron transport. Fast electron spread in radial direction(figure (a) and (d)). Figure (b) and (e) show the axial electric field due to charge separation directed away from relativistic critical density surface (between $4 \mu m$ and $6 \mu m$). The dotted line in (b) shows the fast electron plane of injection.

The next stage of fast electron transport is shown in figure 5.5. Fast electrons travelling along the surface, are deflected towards low density coronal plasma by thermo-electric magnetic fields produced by the long pulse laser (figure 5.5(a) at 0.6 ps). Also, as the fast electrons travel in the coronal plasma shown in figure 5.5(d) (time: 0.9 ps), the Weibel instability [Weibel, 1959] causes strong filamentation of fast electrons and produces large self-generated magnetic fields. Each of these filaments contains a fast electron current at the core surrounded by return current supplied by the background plasma. The typical width of these filaments is $\sim 1 \mu m$. The lower limit for growth of the Weibel-like filamentation instability for fast electron beam having parallel (V_z) and perpendicular (V_\perp) velocities in a cold plasma background can be derived using kinetic as well as fluid models [Bret and Deutsch, 2006, Silva et al., 2002].

$$\frac{n_{fast}}{n_{plasma}} > \gamma_{fast} \frac{V_{\perp}^2}{V_z^2} \quad (5.6)$$

where n_{fast}/n_{plasma} is the ratio of fast electron density to background plasma density, γ_{fast} is the relativistic Lorentz factor for fast electrons. Thus, for a given set of fast electron beam parameters, the Weibel instability is more likely to grow in under-dense plasma compared to over-dense plasma. In our simulations, stronger filamentation of electron beam in the under-dense background plasma can be clearly seen from figure 5.5(d).

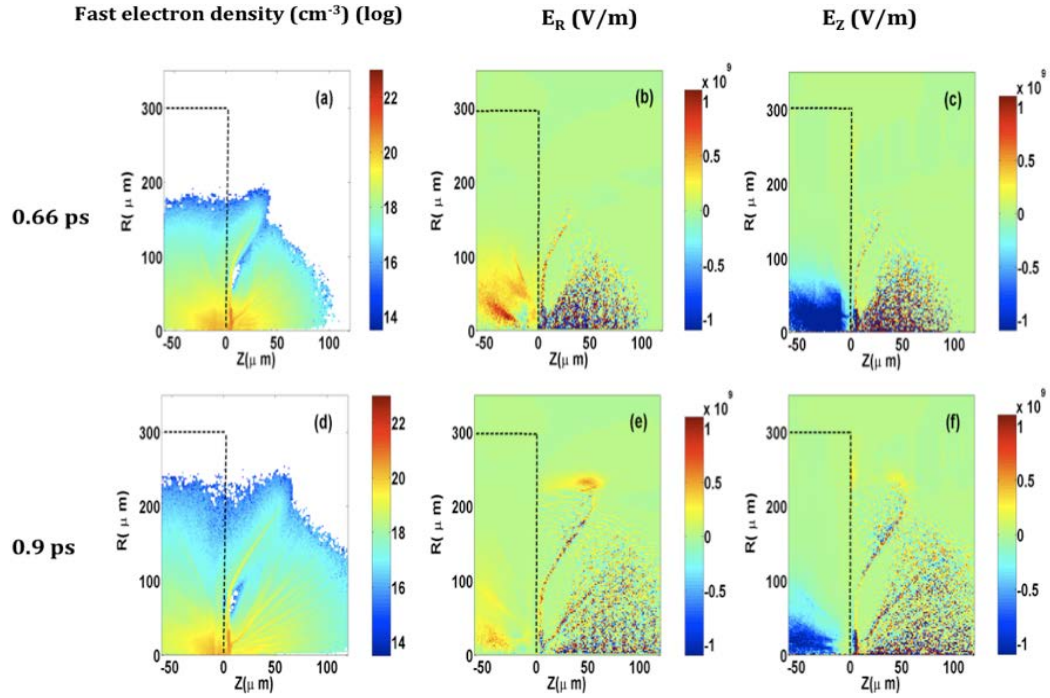


Figure 5.5: Early stages of fast electron transport. Dotted line represents target edge. (a) At 0.66 ps, some of the fast electrons are traveling back into coronal plasma. Also, deflection of fast electrons moving along the target front surface by magnetic field can be seen at $R \sim 100 \mu m$. At 0.9 ps excitation of radial electric field with peak magnitude of 1×10^9 V/m is seen at $(Z, R) \sim (60, 240) \mu m$ in figure 4(e) .

Fast electrons travelling in the coronal plasma eventually reach the low-density plasma region where their density becomes comparable with the coronal plasma density ($n_{fast}/n_{plasma} \sim 0.4$). This excites strong electrostatic fields due to

charge separation (see figure 5.5(e)) at the coronal plasma transverse boundary near $(Z, R) \sim (60, 240) \mu m$. The peak value of this electric field is about 10^9 V/m. Also, it should be noted that initially the radial component of the electric field, E_R ($\sim 1 \times 10^9$ V/m) is higher than the axial component, E_Z ($\sim 3 \times 10^8$ V/m) since these fast electrons are mainly moving in the radial direction.

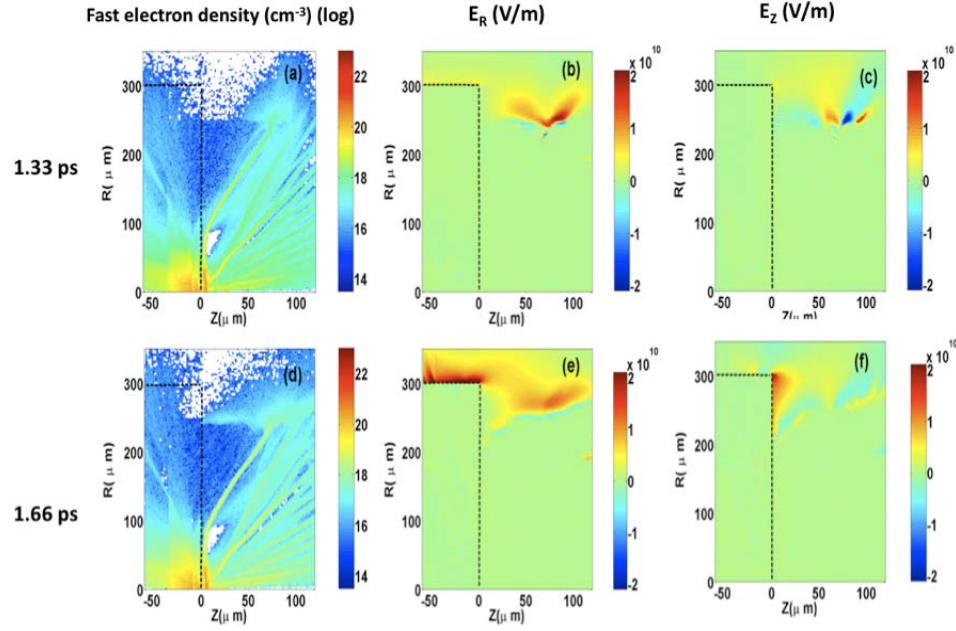


Figure 5.6: Fast electron refluxing in the coronal plasma back to solid target. At 1.33 ps, fast electrons filament splitting in axial direction (Z -direction) can be seen at $(Z, R) \sim (70, 260) \mu m$ in (a) accompanied by excitation of axial electric field of alternating polarity (c). This field splits the beam in a axial direction. (d) Fast electrons are pulled back to the target at $R \sim 250 \mu m$ (time = 1.66 ps)

As fast electrons move further into the under-dense plasma towards the transverse plasma boundary, the local fast electron density becomes greater than the background plasma density. Interesting dynamics of axial electric field (E_Z) are seen at late time (figure 5.6(c)). The excited axial electric field now becomes comparable to the radial electric fields. The peak magnitude of the electric field in either direction is around 2×10^{10} V/m. Its orientation is such that fast electrons initially travelling in the radial direction are now deflected by the electric field into the axial direction. Thus, a fraction of the fast electrons in the coronal plasma now start traveling back toward the solid target as can be clearly seen in the

fast electron density plots in figure 5.6(d). The location of region of reflection where these fields are excited in the coronal plasma depends upon the pre-plasma scale length in the transverse (radial) direction which, in turn, would depend upon energy in pre-pulse, long pulse laser spot size, etc. In addition, figure 5.6(e) and 5.6(f) also show the occurrence of strong electric fields at target edges, arising due to the transverse loss of fast electrons from the target. These fields contribute towards pulling back some of the fast electrons which are initially traveling away from the target in coronal plasma.

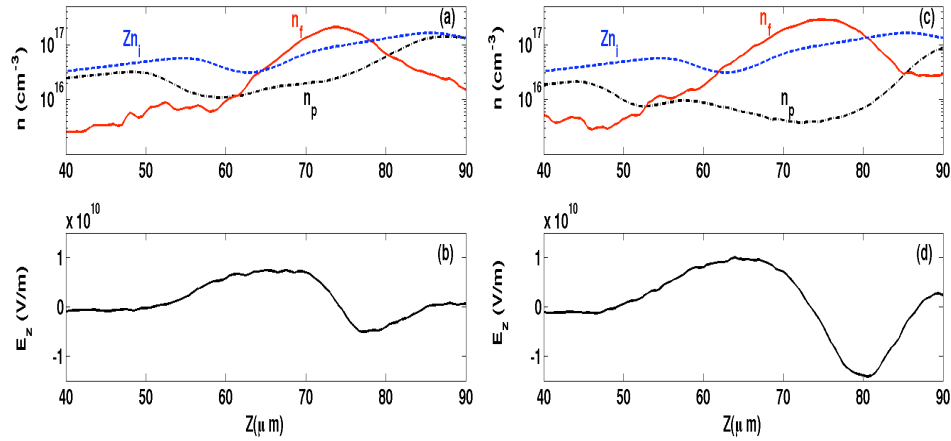


Figure 5.7: Axial line out at $R = 260 \mu m$ of various density profiles and axial electric field (E_z) at 1.25ps and 1.33ps. (a), (c): Red (solid), blue (dash-dotted) and black (dotted) lines represent fast electrons, ions and background plasma electron densities respectively. (b), (d): The corresponding axial electric field of alternate polarity is directed towards the center of fast electron beam ($Z \sim 75 \mu m$) that pulls electrons away from the center.

The growth and polarity of axial electric field, which is important for axial (along Z-direction) diverting of the beam, can be explained with the help of figure 5.7. Figure 5.7 shows the axial line out at $R = 260 \mu m$ of the axial electric field along with the density of fast electrons (n_f), background plasma electrons (n_p) and ions ($Z_i n_i$) at 1.25 ps and 1.33 ps. Note that the peak fast electron density is about 10^{17} cm^{-3} whereas the initial background plasma density is of the order of 10^{16} cm^{-3} . As the fast electron density is greater than background plasma density, background electrons are pushed aside creating net positive charge surrounding the negative

charge of fast electrons. This is apparent from the dip in the background plasma density profiles (black dotted curve) in figure 5.7(a) ($Z=70 \mu m$). We now have axial electric field with alternating polarity. The direction of this electric field is such that the fast electrons are pulled into the axial direction from both sides. The diverting of the beam pushes background plasma electrons further away leading to the enhancement of axial electric field. Note that the dip in the background plasma density has increased with minimum plasma density dropping from 10^{16} cm^{-3} at 1.25 ps to $5 \times 10^{15} \text{ cm}^{-3}$ at 1.33 ps. This creates a positive feedback mechanism, which produces the axial field to deflect some of the fast electrons back towards the target.

Later time (3ps) simulations (see figure 5.8(a)) show the fast electrons entering the Copper layer at a radial location of around $250 \mu m$. Figure 5.8(b) shows the time integrated radial line out of the number of fast electrons passed through the copper layer. While counting these electrons we have only considered the fast electrons having energy greater than 20 keV i.e. only those capable of producing Cu $K\alpha$ x-rays. The increase in fast electron number at $R \sim 250 \mu m$ in figure 5.8(b) is consistent with the 400-500 μm diameter outer ring seen in the experiment.

The robustness of the proposed mechanism for annular ring structure formation is tested by running additional simulations with different divergence angles for the injected fast electron beams : 10° and 60° (see figure 5.9). In all these simulations we see fast electron reflection near the transverse plasma vacuum boundary where the plasma density drops below the fast electron density. The radius of the ring observed in the simulations lies in the range of 220 to 270 μm , which is again consistent with the experimentally observed ring radius.

Finally we compared the above results with a case that did not have a pre-formed plasma. Extremely small pre-plasma was added in front of the target, consistent with the pre-pulse expected from the short pulse laser. As can be seen in figure 5.10(a), fast electrons travelling along the target front surface accumulate at the target edges due to the sheath fields produced by the lateral escape of fast electrons. The radial line out of time-integrated number of electrons passed through the Cu layer shows a small bump at the target edge (figure 5.10(b)) ($R \sim$

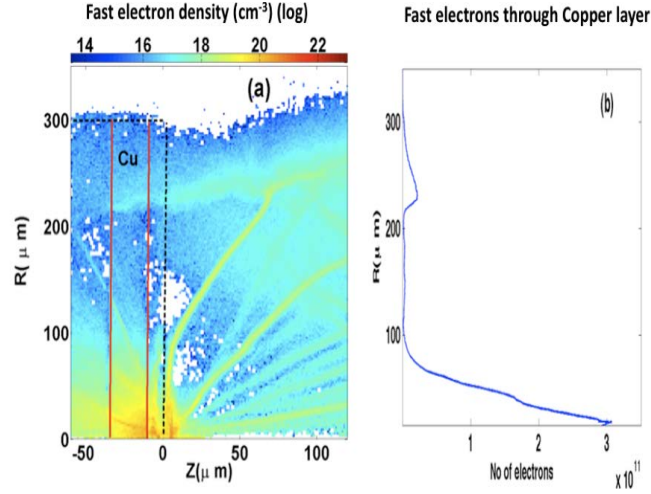


Figure 5.8: Later time (3 ps) simulation results for fast electron transport in presence of pre-plasma. (a) Reflected fast electrons passing through the copper layer (region between red lines) can be seen at $R \sim 250 \mu m$. (b) Radial profile of the total number of fast electrons (energy, $E > 20$ keV) passing through the copper (time integrated). The small bump around $R \sim 250 \mu m$ is consistent with outer radius of ring observed in the experiment.

$300 \mu m$). However, no ring-like structure was seen in this simulation at $R \sim 250 \mu m$, which is consistent with the experimental observation where $K\alpha$ emission was seen mainly from the central region (figure 5.10(b)). We have confirmed that the small bump seen close to $R \sim 300 \mu m$ is only due to the reflection at target edge by performing additional LSP simulations using extended transverse dimension.

5.4 Conclusions

Modeling with radiation hydrodynamic and hybrid-PIC code is performed to explain the ring-like Cu $K\alpha$ x-ray emission arising from fast electron transport in presence of the long scale pre-plasma and thermoelectric B-fields produced by 1 J level long pulse irradiation. Simulations suggest that during early stage of electron transport, some of the fast electrons are pulled back into coronal plasma due to strong electric and magnetic fields at interaction region. Also, azimuthal magnetic field, generated during long pulse interaction deflects the fast electrons travelling along the target surface into coronal plasma. Filamentation of fast electrons occurs

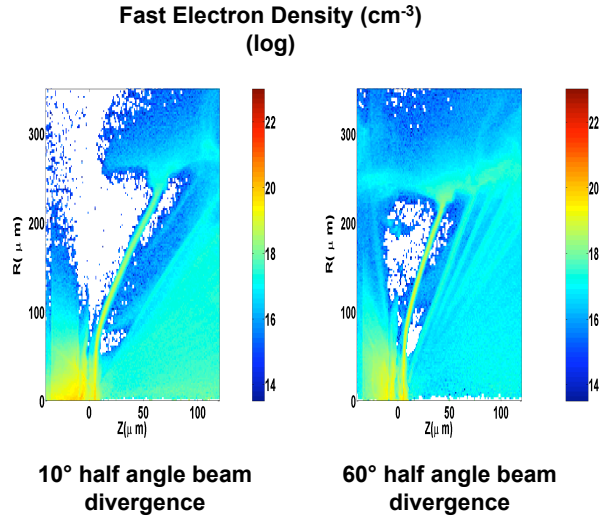


Figure 5.9: Fast electron density comparison at 1.8 ps for 10° and 60° half angle beam divergence. Note that the thick aluminum layer behind Copper is excluded in these simulations.

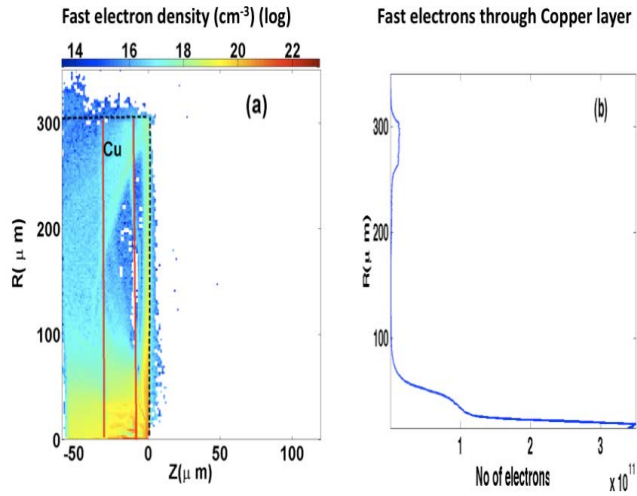


Figure 5.10: Later time (3ps) results of without pre-plasma simulations. (a) Fast electron density at 3 ps. Reflection of electrons from target edge can be seen at $R=300 \mu m$. (b) total number of fast electrons (time integrated) through copper doesn't show the annular ring-like structure seen in the pre-plasma case.

as they travel further into low-density corona. Strong electrostatic fields are excited near the transverse plasma-vacuum boundary where fast electron density becomes comparable with background plasma density. In later stages, when fast electrons

density becomes greater than background density, the strong excitation of axial electrostatic fields lead to refluxing of these electrons back to the target. This explains the outer ring structure in the Cu $K\alpha$ emission spot seen in the experiment. Thus, plasma density gradient in the transverse (radial) direction, fast electron density and energy are the important deciding factors for the occurrence of such a ring structure.

Thus, in this chapter we demonstrate one of the effects of long scale length pre-formed plasma on the fast electrons transport. In addition to this, the reduction in coupling of forward going fast electrons flux due to presence of large pre-formed plasma can pose a serious threat to the prospects of electron fast ignition scheme. Detail study of this topic is necessary in the future work.

Chapter 5 uses material from the following publication and the dissertation author was the primary investigation and first author of the publication :

B.S.Paradkar, M.S. Wei, T. Yabuuchi, R. B. Stephens, J. T. Larsen and F. N. Beg, “Numerical modeling of fast electrons transport in short pulse laser-solid interactions with long scale-length pre-formed plasma”, *Plasma Physics and Controlled Fusion* **52** 125003, 2010.

Chapter 6

Conclusions

In last five chapters we have discussed the influence of pre-formed plasma on relativistic fast electrons generation and transport in laser-solid interaction. This problem is of considerable importance, especially for successful realization of the fast ignition concept of Inertial Confinement Fusion. Also, fundamental understanding of this topic is very important for the interpretation of experimental results in almost all of the laser-solid interactions. We approached this problem both numerically and analytically. Numerical calculations were mainly performed with the help of PIC code LSP [Welch et al., 2001, 2006]. The summary, important conclusions and scope for future work in this topic will be discussed in this chapter.

6.1 Summary and Conclusions

- In chapter three and four we studied the problem of fast electrons generation in presence of pre-formed plasma. The problem is studied systematically by performing PIC simulations for wide range of pre-formed plasma scale-lengths ($1\text{-}15\mu m$) and laser intensities ($10^{19}\text{-}10^{21}$ W/cm²), relevant to present day experiments. We showed that long scale-length pre-formed plasma can result in generation of very high energetic electrons with energies greater than laser ponderomotive energy consistent with the experimental observations. Detailed investigation showed that the ambipolar electric field inside pre-formed plasma plays a crucial role in the fast electrons heating. In chapter

four, we addressed this issue quantitatively by studying the dynamics of electron in presence of longitudinal electrostatic potential well (for a constant electric field) and a plain electromagnetic wave. This mechanism suggests that electron motion in laser radiation becomes stochastic due to the presence of longitudinal electrostatic potential well. The stochasticity is introduced when the electron bounce time inside the potential becomes comparable with the laser time period. Analytical calculations and numerical simulations showed that the electrons initially placed inside the finite depth potential well can indeed escape with energies greater than the laser ponderomotive energy in a deeply stochastic regime.

- In chapter five, we discussed the effect of pre-formed plasma on the fast electrons transport. In particular, we simulated one specific experiment where presence of long pre-formed plasma in front of the solid target resulted in a characteristic annular ring-like transport of fast electrons. It was shown that the reflection of backward going (with reference to laser propagation) electrons due to the excitation of sheath fields inside the pre-formed plasma is responsible for such transport. This provided indirect evidence of backward going fast electrons in the pre-formed plasma in laser-solid interactions. Such electrons going in the backward directions will not be useful since it will result in reduction of coupling of the fast electrons into the dense core.

Clearly this thesis demonstrates that the presence of pre-formed plasma can significantly alter the laser-solid interaction at relativistic intensities. The presence of such plasma of long density scale-length can seriously hamper the prospects of Fast Ignition. On the other hand, the applications like electron-positron pair productions may find long pre-formed plasma favorable due to the production of very energetic electrons with energies well beyond laser ponderomotive potential.

6.2 Future Work

One of the obvious extension of this work would be to investigate this problem in 2-D and 3-D cases. Although the PIC simulations for higher dimensions

can be computationally very demanding, it is important to analyze the importance of the mechanism proposed in this thesis for these cases. The influence of laser filamentation, self-focussing on this heating mechanism needs a detailed investigation. Again, analyzing single electron motion in 2-D/3-D can be a very rewarding approach from the physics understanding point of view.

In the proposed heating mechanism, the stochasticity is introduced in two ways : 1) by counter-propagating E.M. waves 2) by motion of electron inside the potential well in the presence of E.M. wave. The second problem is addressed analytically in this thesis. But it would be interesting to investigate further the introduction of stochasticity by counter-propagating E.M. waves and it's implications on overall heating of pre-formed plasma electrons.

Appendix A

Derivation of Poincare Mapping equations 4.9 and 4.10

Using standard normalization described in the earlier chapters, the constants of motion in the perpendicular and parallel direction with respect to laser propagation for the laser vector potential $a(t, z)$ and constant longitudinal electric field E_z can be expressed as

$$\hat{P}_\perp - a(t, z) = 0 \quad (\text{A.1})$$

$$\gamma - \hat{P}_z - E_z \tau = \delta_0 \quad (\text{A.2})$$

Here, $\hat{P}_\perp = \gamma V_\perp$ and $\hat{P}_z = \gamma V_z$ are the normalized momenta in the perpendicular and parallel directions. Note that $\tau = t - z$ is the phase-slip of the electron with respect to electromagnetic wave. Also, we have assumed zero initial perpendicular momentum and $\delta_0 = (\gamma - \hat{P}_z)|_{\tau=0} = \gamma_A / [\gamma_z (1 + V_z)]$. Here $\gamma_A = \sqrt{1 + \hat{P}_\perp^2}$ and $\gamma_z = 1/\sqrt{1 - V_z^2}$. Therefore, for the relativistic electron δ_0 simplifies to $\delta_0 \simeq \gamma_A/2\gamma_z$. Combining Eq. (A.2) with the equation for total kinetic energy of the electron i.e. $\gamma^2 = 1 + \hat{P}_\perp^2 + \hat{P}_z^2$ we get

$$\gamma = \frac{1}{2} \left[\frac{1 + \hat{P}_\perp^2}{\delta_0 + E_z \tau} + (\delta_0 + E_z \tau) \right] \quad (\text{A.3})$$

$$\hat{P}_z = \frac{1}{2} \left[\frac{1 + \hat{P}_\perp^2}{\delta_0 + E_z \tau} - (\delta_0 + E_z \tau) \right] \quad (\text{A.4})$$

Now, the electron motion can be described using Eq. (A.2) as

$$\frac{dz}{d\tau} = \frac{dz/dt}{d\tau/dt} = \frac{V_z}{1 - V_z} = \frac{\hat{P}_z}{\delta_0 + E_z \tau} \quad (\text{A.5})$$

Substituting \hat{P}_z from Eq. (A.4) we get

$$\frac{dz}{d\tau} = \frac{1}{2} \left[\frac{\gamma_A^2}{(\delta_0 + E_z \tau)^2} - 1 \right] \quad (\text{A.6})$$

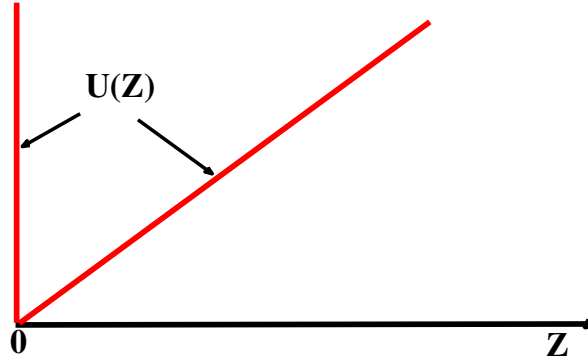


Figure A.1: Electrostatic potential well chosen for the analysis of electron motion. Perfectly reflecting ‘potential wall’ is assumed at $z = 0$.

At this point, we introduce the electrostatic potential well $U(z)$ as shown above with constant longitudinal electric field E_z . Since we are only interested in the physics of phase randomization of the electron, we have assumed infinite potential wall at $z = 0$ for the case of simplicity and clarity. This means that the electron is re-injected in the potential well at $z = 0$, preserving its energy.

Now, the motion of the electron, present initially at $z = 0$ and time, $t = t_0$ inside such potential well can be described by integrating Eq. (A.6) as

$$z = \frac{1}{2} \int_0^\tau \frac{[\gamma_A(t_0 + \tau')]^2}{(\delta_0 + E_z \tau')^2} d\tau' - \frac{\tau}{2} \quad (\text{A.7})$$

Therefore, the time t_1 when the electron returns back to $z = 0$ can be expressed as

$$t_1 - t_0 = \int_0^{t_1 - t_0} \frac{[\gamma_A(t_0 + \tau')]^2}{(\delta_0 + E_z \tau')^2} d\tau' \quad (\text{A.8})$$

Integrating by parts we get

$$t_1 - t_0 = -\frac{\gamma_A^2(t_1)}{E_z(\delta_0 + E_z(t_1 - t_0))} + \frac{\gamma_A^2(t_0)}{E_z \delta_0} + \frac{1}{E_z} \int_0^{t_1 - t_0} \frac{\frac{d}{d\tau'} [\gamma_A^2(t_0 + \tau')]}{\delta_0 + E_z \tau'} d\tau' \quad (\text{A.9})$$

Considering the dynamic for the ultra-relativistic electron ($\delta_0 = O(\epsilon) \ll 1$) we can simplify the first two terms of the RHS of the above equation as follows:

$$\begin{aligned} \frac{\gamma_A^2(t_0)}{E_z \delta_0} &= \frac{\gamma(t_0) [1 + V_z(t_0)]}{E_z} \sim \frac{2\gamma(t_0)}{E_z} \\ \frac{\gamma_A^2(t_1)}{E_z [\delta_0 + E_z(t_1 - t_0)]} &= \frac{\gamma(t_1) [1 + V_z(t_1)]}{E_z} \sim O(\epsilon) \end{aligned}$$

Note that $V_z(t_0) \sim 1$ and $V_z(t_1) \sim -1$ are used in the above equations. Also, the term $\frac{\gamma_A^2(t_0)}{E_z \delta_0}$ is proportional to the energy of the fast electron. Therefore, introducing the new notation $\hat{G}_0 = \frac{\gamma_A^2(t_0)}{E_z \delta_0}$ we can write Eq. (A.9) as

$$t_1 - t_0 = \hat{G}_0 + \frac{1}{E_z} \int_0^{t_1 - t_0} \frac{\frac{d}{d\tau'} [\gamma_A^2(t_0 + \tau')]}{\delta_0 + E_z \tau'} d\tau' + O(\epsilon) \quad (\text{A.10})$$

The above equation can be rearranged in the form of ‘Chirikov Standard Map’ [Chirikov, 1979] as follows:

$$\hat{G}_1 = \hat{G}_0 + \frac{1}{E_z} \int_0^{t_1 - t_0} \frac{\frac{d}{d\tau'} [\gamma_A^2(t_0 + \tau')]}{\delta_0 + E_z \tau'} d\tau' + O(\epsilon) \quad (\text{A.11})$$

$$t_1 = t_0 + \hat{G}_1 \quad (\text{A.12})$$

Now, for a plain E.M. wave, $\gamma_A^2(t_0 + \tau') = 1 + a_0^2 \cos^2(t_0 + \tau')$, the equation (A.11) reduces to

$$\hat{G}_1 = \hat{G}_0 - \frac{a_0^2}{E_z} \left[\sin(2t_0) \int_0^{t_1-t_0} \frac{\cos(2\tau')}{\delta_0 + E_z \tau'} d\tau' + \cos(2t_0) \int_0^{t_1-t_0} \frac{\sin(2\tau')}{\delta_0 + E_z \tau'} d\tau' \right] + O(\epsilon) \quad (\text{A.13})$$

Finally, simplifying the integrals on the RHS and neglecting the higher order terms ($O(\epsilon)$), we recover the mapping equation (4.9).

$$\hat{G}_1 = \hat{G}_0 - \frac{a_0^2}{E_z^2} \left\{ \frac{\pi}{2} \cos(2t_0) + \left[\ln \left(\frac{E_z}{2\delta_0} \right) - C \right] \sin(2t_0) \right\} + O(\epsilon) \quad (\text{A.14})$$

Here, C is the Euler's constant. Finally expressing δ_0 in terms of \hat{G}_0 we can write recursive equation described by equation (4.9) and (4.10).

$$\hat{G}_i = \hat{G}_{i-1} - \left(\frac{a_0}{E_z} \right)^2 \left\{ \frac{\pi}{2} \cos(2t_{i-1}) + \left[\ln \left(\frac{\hat{G}_{i-1} E_z^2}{2(\gamma_A(t_{i-1}))^2} \right) - C \right] \sin(2t_{i-1}) \right\} \quad (\text{A.15})$$

$$t_i = t_{i-1} + \hat{G}_i \quad (\text{A.16})$$

Bibliography

- K. Adumi, KA Tanaka, T. Matsuoka, T. Kurahashi, T. Yabuuchi, Y. Kitagawa, R. Kodama, K. Sawai, K. Suzuki, K. Okabe, et al. Characterization of preplasma produced by an ultrahigh intensity laser system. *Physics of Plasmas*, 11:3721, 2004.
- H. Alfvén. On the motion of cosmic rays in interstellar space. *Physical Review*, 55(5):425, 1939.
- F. Amiranoff, K. Eidmann, R. Sigel, R. Fedosejevs, A. Maaswinkel, Y. Teng, JD Kilkenny, JD Hares, DK Bradley, BJ MacGowan, et al. The evolution of two-dimensional effects in fast-electron transport from high-intensity laser-plasma interactions. *Journal of Physics D: Applied Physics*, 15:2463, 1982.
- AA Andreev, K.Y. Platonov, T. Okada, and S. Toraya. Nonlinear absorption of a short intense laser pulse in a nonuniform plasma. *Physics of Plasmas*, 10:220, 2003.
- J. Angus and S. Krasheninnikov. Energy gain of free electron in pulsed electromagnetic plane wave with constant external magnetic fields. *Physics of Plasmas*, 16:113103, 2009.
- SD Baton, M. Koenig, J. Fuchs, A. Benuzzi-Mounaix, P. Guillou, B. Loupiau, T. Vinci, L. Gremillet, C. Rousseaux, M. Drouin, et al. Inhibition of fast electron energy deposition due to preplasma filling of cone-attached targets. *Physics of Plasmas*, 15:042706, 2008.
- FN Beg, AR Bell, AE Dangor, CN Danson, AP Fews, ME Glinsky, BA Hammel, P. Lee, PA Norreys, and M. Tatarakis. A study of picosecond laser–solid interactions up to 10^{19} W/cm². *Phys. Plasmas*, 4:447, 1997.
- AR Bell, JR Davies, S. Guerin, and H. Ruhl. Fast-electron transport in high-intensity short-pulse laser-solid experiments. *Plasma physics and controlled fusion*, 39:653, 1997.

- AR Bell, JR Davies, and SM Guerin. Magnetic field in short-pulse high-intensity laser-solid experiments. *Physical Review E*, 58(2):2471, 1998.
- C.K. Birdsall and A.B. Langdon. *Plasma physics via computer simulation*. McGrawHill publications, 1985.
- A. Bourdier, D. Patin, and E. Lefebvre. Stochastic heating in ultra high intensity laser-plasma interaction. *Laser and Particle Beams*, 25(1):169, 2007.
- SI Braginskii. Transport processes in a plasma. *Reviews of plasma physics*, 1:205, 1965.
- A. Bret and C. Deutsch. Stabilization of the filamentation instability and the anisotropy of the background plasma. *Physics of plasmas*, 13:022110, 2006.
- F. Brunel. Not-so-resonant, resonant absorption. *Physical review letters*, 59(1):52–55, 1987.
- MDJ Burgess, B. Luther-Davies, and KA Nugent. An experimental study of magnetic fields in plasmas created by high intensity one micron laser radiation. *Physics of Fluids*, 28:2286, 1985.
- H. Cai, K. Mima, A. Sunahara, T. Johzaki, H. Nagatomo, S. Zhu, and XT He. Prepulse effects on the generation of high energy electrons in fast ignition scheme. *Physics of Plasmas*, 17:023106, 2010.
- F. Califano, F. Pegoraro, and S. V. Bulanov. Spatial structure and time evolution of the weibel instability in collisionless inhomogeneous plasmas. *Phys. Rev. E*, 56:963, 1997.
- PJ Catto and R.M. More. Sheath inverse bremsstrahlung in laser produced plasmas. *Physics of Fluids*, 20:704, 1977.
- H. Chen and S.C. Wilks. Evidence of enhanced effective hot electron temperatures in ultraintense laser-solid interactions due to reflexing. *Laser and Particle Beams*, 23(4):411, 2005.
- SN Chen, G. Gregori, PK Patel, H.K. Chung, RG Evans, RR Freeman, E.G. Saiz, SH Glenzer, SB Hansen, FY Khattak, et al. Creation of hot dense matter in short-pulse laser-plasma interaction with tamped titanium foils. *Physics of Plasmas*, 14:102701, 2007.

- B.V. Chirikov. A universal instability of many-dimensional oscillator systems. *Physics reports*, 52(5):263–379, 1979.
- C. Courtois, A.C. La Fontaine, O. Landoas, G. Lidove, V. Méot, P. Morel, R. Nuter, E. Lefebvre, A. Boscheron, J. Grenier, et al. Effect of plasma density scale length on the properties of bremsstrahlung x-ray sources created by picosecond laser pulses. *Physics of Plasmas*, 16:013105, 2009.
- JE Crow, PL Auer, and JE Allen. The expansion of a plasma into a vacuum. *Journal of Plasma Physics*, 14:65–76, 1975.
- JR Davies, JS Green, and PA Norreys. Electron beam hollowing in laser–solid interactions. *Plasma physics and controlled fusion*, 48:1181, 2006.
- IY Dodin and NJ Fisch. Correction to the alfvén-lawson criterion for relativistic electron beams. *Physics of plasmas*, 13:103104, 2006.
- R.G. Evans. Modelling electron transport for fast ignition. *Plasma Physics and Controlled Fusion*, 49:B87, 2007.
- R. Fabbro and P. Mora. Hot electrons behavior in laser-plane target experiments. *Physics Letters A*, 90(1-2):48–50, 1982.
- E. Fermi. On the origin of the cosmic radiation. *Physical Review*, 75(8):1169, 1949.
- DW Forslund and JU Brackbill. Magnetic-field-induced surface transport on laser-irradiated foils. *Physical Review Letters*, 48(23):1614–1617, 1982.
- EG Gamaliy and VT Tikhonchuk. Anomalous skin effect. *JETP Lett*, 48:453–455, 1988.
- VN Goncharov, OV Gotchev, E. Vianello, TR Boehly, JP Knauer, PW McKenty, PB Radha, SP Regan, TC Sangster, S. Skupsky, et al. Early stage of implosion in inertial confinement fusion: Shock timing and perturbation evolution. *Physics of plasmas*, 13:012702, 2006.
- S.P. Hatchett, C.G. Brown, T.E. Cowan, E.A. Henry, J.S. Johnson, M.H. Key, J.A. Koch, A.B. Langdon, B.F. Lasinski, R.W. Lee, et al. Electron, photon, and ion beams from the relativistic interaction of petawatt laser pulses with solid targets. *Physics of Plasmas*, 7:2076, 2000.
- PA Jaanimagi, NA Ebrahim, NH Burnett, and C. Joshi. Return-current electron

- streams in high-intensity laser target interaction. *Applied Physics Letters*, 38(10):734–736, 1981.
- M. Kaluza, J. Schreiber, M.I.K. Santala, G.D. Tsakiris, K. Eidmann, J. Meyer-ter Vehn, and KJ Witte. Influence of the laser prepulse on proton acceleration in thin-foil experiments. *Physical review letters*, 93(4):45003, 2004.
- PL Kelley. Self-focusing of optical beams. *Physical Review Letters*, 15(26):1005–1008, 1965.
- AJ Kemp, Y. Sentoku, and M. Tabak. Hot-electron energy coupling in ultraintense laser-matter interaction. *Physical Review E*, 79(6):066406, 2009.
- AJ Kemp, BI Cohen, and L. Divol. Integrated kinetic simulation of laser-plasma interactions, fast-electron generation, and transport in fast ignition. *Physics of Plasmas*, 17:056702, 2010.
- MH Key, JC Adam, KU Akli, M. Borghesi, MH Chen, RG Evans, RR Freeman, H. Habara, SP Hatchett, JM Hill, et al. Fast ignition relevant study of the flux of high intensity laser-generated electrons via a hollow cone into a laser-imploded plasma. *Physics of Plasmas*, 15:022701, 2008.
- JC Kieffer, H. Pépin, M. Piché, JP Matte, TW Johnston, P. Lavigne, F. Martin, and R. Decoste. Hot-electron energy deposition in co-₂-laser-irradiated targets consistent with magnetic-field-induced surface transport. *Physical review letters*, 50(14):1054–1057, 1983.
- JA Koch, MH Key, RR Freeman, SP Hatchett, RW Lee, D. Pennington, RB Stephens, and M. Tabak. Experimental measurements of deep directional columnar heating by laser-generated relativistic electrons at near-solid density. *Physical Review E*, 65(1):016410, 2001.
- W.L. Kruer. *The physics of laser plasma interactions*, volume 73. Westview Pr, 2003.
- WL Kruer and K. Estabrook. J \times b heating by very intense laser light. *Physics of Fluids*, 28:430, 1985.
- L.D. Landau and E.M. Lifshitz. *Course of theoretical physics: The classical theory of fields*, volume 2. Butterworth-Heinemann, 2010.
- HJ Lee, KH Pae, H. Suk, and SJ Hahn. Enhancement of high-energy ion generation

- by preplasmas in the interaction of an intense laser pulse with overdense plasmas. *Physics of Plasmas*, 11:1726, 2004.
- YT Lee and RM More. An electron conductivity model for dense plasmas. *Physics of Fluids*, 27:1273, 1984.
- E. Lefebvre and G. Bonnaud. Nonlinear electron heating in ultrahigh-intensity-laser-plasma interaction. *Physical Review E*, 55(1):1011, 1997.
- E.P. Liang, S.C. Wilks, and M. Tabak. Pair production by ultraintense lasers. *Physical review letters*, 81(22):4887–4890, 1998.
- A.J. Lichtenberg and M.A. Lieberman. Regular and stochastic motion. *Research supported by the US Department of Energy, US Navy, and NSF. New York, Springer-Verlag (Applied Mathematical Sciences. Volume 38), 1983, 516 p., 38, 1983.*
- B. Luther-Davies, A. Perry, and KA Nugent. $K\alpha$ emission measurements and superthermal electron transport in layered laser-irradiated disk targets. *Physical Review A*, 35(10):4306, 1987.
- AG MacPhee, L. Divol, AJ Kemp, KU Akli, FN Beg, CD Chen, H. Chen, DS Hey, RJ Fedosejevs, RR Freeman, et al. Limitation on prepulse level for cone-guided fast-ignition inertial confinement fusion. *Physical review letters*, 104(5):55002, 2010.
- P. Maine, D. Strickland, P. Bado, M. Pessot, and G. Mourou. Generation of ultrahigh peak power pulses by chirped pulse amplification. *Quantum Electronics, IEEE Journal of*, 24(2):398–403, 1988.
- C.E. Max, J. Arons, and A.B. Langdon. Self-modulation and self-focusing of electromagnetic waves in plasmas. *Physical Review Letters*, 33(4):209–212, 1974.
- C.E. Max, W.M. Manheimer, and JJ Thomson. Enhanced transport across laser generated magnetic fields. *Physics of Fluids*, 21:128, 1978.
- R. Mishra, Y. Sentoku, and AJ Kemp. Hot electron generation forming a steep interface in superintense laser-matter interaction. *Physics of Plasmas*, 16:112704, 2009.
- P. Mora and R. Pellat. Self-similar expansion of a plasma into a vacuum. *Physics of Fluids*, 22:2300, 1979.

- R. Nuter, L. Gremillet, P. Combis, M. Drouin, E. Lefebvre, A. Flacco, and V. Malka. Influence of a preplasma on electron heating and proton acceleration in ultraintense laser-foil interaction. *Journal of Applied Physics*, 104(10):103307–103307, 2008.
- H.S. Park, DM Chambers, H.K. Chung, RJ Clarke, R. Eagleton, E. Giraldez, T. Goldsack, R. Heathcote, N. Izumi, MH Key, et al. High-energy $k\alpha$ radiography using high-intensity, short-pulse lasers. *Physics of plasmas*, 13:056309, 2006.
- A. Pukhov, Z.M. Sheng, and J. Meyer-ter Vehn. Particle acceleration in relativistic laser channels. *Physics of Plasmas*, 6:2847, 1999.
- Y. Sentoku, V.Y. Bychenkov, K. Flippo, A. Maksimchuk, K. Mima, G. Mourou, ZM Sheng, and D. Umstadter. High-energy ion generation in interaction. of short laser pulse with high-density plasma. *Applied Physics B: Lasers and Optics*, 74(3):207–215, 2002.
- Z.M. Sheng, K. Mima, J. Zhang, and J. Meyer-ter Vehn. Efficient acceleration of electrons with counterpropagating intense laser pulses in vacuum and underdense plasma. *Physical Review E*, 69(1):016407, 2004.
- M. Sherlock. Universal scaling of the electron distribution function in one-dimensional simulations of relativistic laser-plasma interactions. *Physics of Plasmas*, 16:103101, 2009.
- L.O. Silva, R.A. Fonseca, J.W. Tonge, W.B. Mori, and J.M. Dawson. On the role of the purely transverse weibel instability in fast ignitor scenarios. *Physics of Plasmas*, 9:2458, 2002.
- RB Stephens, RA Snavely, Y. Aglitskiy, F. Amiranoff, C. Andersen, D. Batani, SD Baton, T. Cowan, RR Freeman, T. Hall, et al. K_{α} fluorescence measurement of relativistic electron transport in the context of fast ignition. *Physical Review E*, 69(6):066414, 2004.
- D. Strickland and G. Mourou. Compression of amplified chirped optical pulses. *Optics Communications*, 55(6):447–449, 1985.
- G.Z. Sun, E. Ott, YC Lee, and P. Guzdar. Self-focusing of short intense pulses in plasmas. *Physics of Fluids*, 30:526, 1987.
- M. Tabak, J. Hammer, M.E. Glinsky, W.L. Kruer, S.C. Wilks, J. Woodworth,

- E.M. Campbell, M.D. Perry, and R.J. Mason. Ignition and high gain with ultrapowerful lasers. *Physics of Plasmas*, 1(5):1626, 1994.
- T. Tajima and JM Dawson. Laser electron accelerator. *Physical Review Letters*, 43(4):267–270, 1979.
- RPJ Town, C. Chen, LA Cottrill, MH Key, WL Kruer, AB Langdon, BF Lasinski, RA Snavely, CH Still, M. Tabak, et al. Simulations of electron transport for fast ignition using lsp. *Nuclear Instruments and Methods in Physics Research Section A: Accelerators, Spectrometers, Detectors and Associated Equipment*, 544(1-2): 61–66, 2005.
- L. Van Woerkom, KU Akli, T. Bartal, FN Beg, S. Chawla, CD Chen, E. Chowdhury, RR Freeman, D. Hey, MH Key, et al. Fast electron generation in cones with ultraintense laser pulses. *Physics of Plasmas*, 15:056304, 2008.
- J.M. Wallace. Nonlocal energy deposition in high-intensity laser-plasma interactions. *Physical review letters*, 55(7):707–710, 1985.
- J.M. Wallace, J.U. Brackbill, and D.W. Forslund. An implicit moment electromagnetic plasma simulation in cylindrical coordinates. *Journal of Computational Physics*, 63(2):434–457, 1986.
- MS Wei, AA Solodov, J. Pasley, RB Stephens, DR Welch, and FN Beg. Study of relativistic electron beam production and transport in high-intensity laser interaction with a wire target by integrated lsp modeling. *Physics of Plasmas*, 15:083101, 2008.
- E.S. Weibel. Spontaneously growing transverse waves in a plasma due to an anisotropic velocity distribution. *Physical Review Letters*, 2(3):83–84, 1959.
- E.S. Weibel. Anomalous skin effect in a plasma. *Physics of Fluids*, 10:741, 1967.
- DR Welch, DV Rose, BV Oliver, and RE Clark. Simulation techniques for heavy ion fusion chamber transport* 1. *Nuclear Instruments and Methods in Physics Research Section A: Accelerators, Spectrometers, Detectors and Associated Equipment*, 464(1-3):134–139, 2001.
- DR Welch, DV Rose, ME Cuneo, RB Campbell, and TA Mehlhorn. Integrated simulation of the generation and transport of proton beams from laser-target interaction. *Physics of plasmas*, 13:063105, 2006.

- SC Wilks, WL Kruer, M. Tabak, and AB Langdon. Absorption of ultra-intense laser pulses. *Physical review letters*, 69(9):1383–1386, 1992.
- SC Wilks, AB Langdon, TE Cowan, M. Roth, M. Singh, S. Hatchett, MH Key, D. Pennington, A. MacKinnon, and RA Snavely. Energetic proton generation in ultra-intense laser–solid interactions. *Physics of Plasmas*, 8:542, 2001.
- PM Woodward and JD Lawson. The theoretical precision with which an arbitrary radiation-pattern may be obtained from a source of finite size. *Electrical Engineers-Part III: Radio and Communication Engineering, Journal of the Institution of*, 95(37):363–370, 1948.
- T. Yabuuchi, BS Paradkar, MS Wei, JA King, FN Beg, RB Stephens, N. Nakanii, M. Hatakeyama, H. Habara, K. Mima, et al. Transport study of intense-laser-produced fast electrons in solid targets with a preplasma created by a long pulse laser. *Physics of Plasmas*, 17:060704, 2010.
- A. Yogo, H. Daido, A. Fukumi, Z. Li, K. Ogura, A. Sagisaka, A.S. Pirozhkov, S. Nakamura, Y. Iwashita, T. Shirai, et al. Laser prepulse dependency of proton-energy distributions in ultraintense laser-foil interactions with an online time-of-flight technique. *Physics of plasmas*, 14:043104, 2007.
- P.H. Yoon. Electromagnetic weibel instability in a fully relativistic bi-maxwellian plasma. *Physics of Fluids B: Plasma Physics*, 1:1336, 1989.